



## Research Article

# Petrology of the meta-mafic rocks from the Lolodorf area, Nyong complex (Southwest Cameroon): implication for the origin and emplacement conditions



Eric José Messi Ottou<sup>1,2</sup> · Sylvestre Martial Ntomba<sup>3</sup> · Benjamin Ntieche<sup>4</sup> · Rufine Christelle Magnekou Takamte<sup>1</sup> · Salomon Bertrant Bisse<sup>1,2</sup> · François Ndong Bidzang<sup>5</sup> · Joseph Mvondo Ondo<sup>1</sup>

Received: 19 April 2022 / Accepted: 20 June 2022

Published online: 09 July 2022

© The Author(s) 2022 **OPEN**

## Abstract

This study presents the new petrology and geochemistry data for the comprehension of the origin and emplacement conditions of the Lolodorf mafic rocks within the Nyong Complex. The meta-mafic rocks consist of fine-grained garnet meta-mafic (FGM) and coarse-grained garnet meta-mafic (CGM) rocks presenting nearly similar mineral composition. They are made up of quartz, plagioclase, garnet orthopyroxene, clinopyroxene, amphibole, opaques, apatite and rutile. They also present recrystallization features such as quartz ribbons, corroded grain mineral, cusped plagioclase boundary and necklace garnets in the matrix. These mineral assemblages suggest that the recrystallization took place under granulite facies condition. The meta-mafic rocks have basaltic and tholeiitic composition like the magmas ( $\text{SiO}_2_{\text{FGM}} = 48.20\text{--}50.70$  wt% and  $\text{SiO}_2_{\text{CGM}} = 46.68\text{--}50.27$  wt% and  $\text{Mg}_{\text{FGM}} = 43.24\text{--}62.27$  and  $\text{Mg}_{\text{CGM}} = 40.85\text{--}69.70$ ) emplaced in the active continental margin context. The low La/Th ratio observed in the FGM and the high La/Th ratio in the CGM together with low Hf content imply that the FGM are reworked plutonic rocks that recorded both high grade partial melting and metamorphism whereas CGM recorded only metamorphism imprints. Thermobarometry results suggest that the partial melting and metamorphic peak occurred around the amphibolite-granulite facies transition. The fine-grained garnet meta-mafic rocks emplaced under pressure estimated at around 2.7–14.89 kbar with temperature interval between 672 and 952 °C while the coarse-grained garnet meta-mafics settled at around 1.5–16.09 kbar and 631–909 °C. The selected amphiboles display low water content (1.92–2.10 wt%) and plot between NNO and NNO + 2 buffers indicating that they crystallized under high oxidizing conditions. These results coupled with previous geochronological study suggest that the FGM may have occurred at the Mesoarchean and have been reworked during Eburnean whereas the CGM may have been formed at the Eburnean.

**Supplementary Information** The online version contains supplementary material available at <https://doi.org/10.1007/s42452-022-05089-7>.

✉ Eric José Messi Ottou, [messi125@yahoo.fr](mailto:messi125@yahoo.fr); [ericjosemessiottou@gmail.com](mailto:ericjosemessiottou@gmail.com) | <sup>1</sup>Department of Earth Sciences, Faculty of Science, The University of Yaoundé I, P.O. Box: 812, Yaoundé, Cameroon. <sup>2</sup>School of Geology and Mining Engineering, The University of Ngaoundéré, P.O. Box: 115, Meiganga, Cameroon. <sup>3</sup>Centre for Geological and Mining Research, Institute for Geological and Mining Research, P.O. Box: 333, Garoua, Cameroon. <sup>4</sup>Geology Laboratory, Department of Biological Sciences, Higher Teacher's Training School, The University of Yaoundé I, P.O. Box: 47, Yaoundé, Cameroon. <sup>5</sup>Laboratory of the Mining Treatment, Institute for Geological and Mining Research, P.O. Box: 4110, Yaoundé, Cameroon.



## Highlights

- (1) The rocks of the study area consists of fine-grained garnet meta-mafic (FGM) and coarse-grained garnet meta-mafic (CGM) rocks presenting partial melting and metamorphic features characterizing the amphibolite-granulite facies transition;
- (2) Fine-grained garnet meta-mafic (FGM) have been reworked during Eburnean whereas coarse-grained garnet meta-mafic (CGM) formed at the Eburnean;
- (3) The partial melting and metamorphic peak occurred around the amphibolite-granulite facies transition between 2.7–14.89 kbar and 672–952 °C for the FGM and around 1.5–16.09 kbar and 631–909 °C for the CGM.

Meta-mafic rocks protolith displays basaltic composition and emplaced at an active continental margin context under high oxidizing conditions.

**Keywords** Meta-mafic rocks · Amphibole-granulite facies transition · Partial melting · Nyong Complex · Cameroon

## 1 Introduction

Mafic rocks are volumetrically minor components of old Precambrian terranes that have provided important tools or contributions to the understanding of the geodynamic processes during early times [1–4]. Furthermore, the mafic rocks as well as large volume of Archean and Proterozoic continental crusts that are affected by partial melting are of much concern for modelling the evolution of recycled Archean continental crust. However, most of individual occurrences of these mafic rocks are attributed to wide-ranging geodynamic context. (1) Precambrian remnants of ophiolites or eclogites or (2) intrusive mafic layers which are often linked to a range of geodynamic context; (3) sills belonging to an oceanic crust in subduction environments; (4) remnants of arc related oceanic crust; (5) remnants of greenstone belts which have sagducted and (6) residual mantle following high degree of partial melting [5–9]. Particularly, controversy exists about the geodynamic context of mafic rocks generations during the Paleoproterozoic time [10, 11]. Two interpretation models have been proposed. First, there is evidence that in many Paleoproterozoic high grade belts, shortening is accommodated by the distributed thickening without real evidence for large-scale thrusting [12–14]. Second, the existence of Paleoproterozoic eclogites interpreted as suture zones indicated that subduction and Phanerozoic or ‘modern’ plate tectonic processes have played since that time [15, 16]. Most of geochemical finger printings in the Paleoproterozoic times are framed in the Phanerozoic tectonic [1, 2, 17]. They are the relative depletion of HFSE (Ta, Nb, Ti, Zr and Hf) on normalised trace element plots of these mafic rocks and the local observation of high pressure meta-mafics so called eclogite relics. Theses finger prints are often widely used as evidence for subduction similar, to that observed in the Phanerozoic arc magmatic

area [18–22]. Furthermore, metasomatism and hydrothermal processes can mobilize HFSE and REE, which are typically thought to be immobile [23–25]. The occurrence of high-pressure rocks without thrust tectonics can be derived both by virtue homogeneous crustal thickening [3, 26, 27] and during extensional context. Despite these findings, caution is advised when using the HFSE anomaly because it can also be caused by interaction with the Sub-Continental Lithospheric Mantel (SCLM) [28] or via crustal contamination [29]. The occurrence of high-pressure rocks does not necessarily imply thrust-dominated tectonics [3]. The Cameroon Craton represents the northern edge of the Congo Craton. It consists of the Ntem complex (NC) and the Nyong complex (NyC) (Fig. 1b, c; [30–33]). The NyC records the Eburnean orogeny that occurred during the collision between the Congo and So Francisco shields (Fig. 1c; [32, 34–36]). The Lolodorf area which is part of the NyC appears as an islet not yet been studied. In this study, the meta-mafic rocks from Lolodorf give an opportunity to assess new petrographical, mineralogical and geochemical data to understand the origin and evolution of the meta-mafic rocks protolith.

## 2 Geological setting

The Eburnean orogeny in Cameroon includes the NyC [33, 38] along the NW boundary of the with NC [33, 38, 39] and Ayna series [40, 41]. However, this Eburnean orogeny has been recorded out of the NyC notably in the Adamawa-Yade domain which appears as relics within the late Neoproterozoic Panafrican fold belt [42–44]. Biotite-hornblende gneiss, commonly known as grey gneiss (or migmatic grey gneiss) of TTG composition, is found in the NyC lithological formations [45–47]. Moreover, orthopyroxene-garnet gneiss with charnockite composition,

garnet-amphibole pyroxenites (metabasites interpreted as remnant eclogitic bodies) [20–22, 48], banded iron formation and magmatic rocks more or less metamorphosed (charnockite, augen metadiorite, metasyenite, granite and dolerite; [35, 37]). These sedimentary and plutonic rocks were remobilized during the Eburnean/Trans Amazonian orogeny due to the collision between the Congo and São Francisco Shields (Fig. 1b; [32, 34, 43]). The field observations and the geochemistry analyses support the derivation of the NyC rocks from the partial melting of the Archean crust [46, 47, 49]. The NyC is mostly characterized by flat lying foliation associated with stretching lineation variably oriented and resulting from the transposition of primary foliation by isoclinal recumbent folds during the second phase of deformation. Locally, large opening folds associated with shear zones disrupt this foliation [35, 44]. The NyC is marked by polycyclic metamorphic evolution with eclogite facies [20, 21] characterized by two deformation phases, synchronous with the emplacement of charnockite and/or migmatization process near the boundary with the NC. It is also marked by high grade granulitic assemblages characterized by polygonal fine-grained quartzo-feldspathic minerals suggesting the recrystallization process under high temperature and by the presence of corona rims illustrating a static evolution under granulite to amphibolite facies conditions [50, 51]. From eclogite phase, retrogressive phases continue down to greenschist facies conditions locally overprinted [40, 47]. Previous works on the NyC suggested that the second phase of deformation is retrograde and belongs to the Eburnean nappe formations which were transported

eastward onto the NC under the amphibolitic condition [33] and dated at ca 2050 Ma [34, 40, 46]. The critical isotopic data (Sm–Nd and  $T_{DM}$  data [46, 49]) indicate that the Nyong rocks have protolith with both an Archean age and the contribution of juvenile mantle materials. Due to the fact that the eclogitic metamorphism has been dated at ca 2.09 Ga ([20], SHRIMP U–Pb/Zr), the NyC area has been considered as one of the oldest suture zone or subducted slab so far recorded in the world [20]. The rocks of the NyC have also experienced a major late migmatitic, granulitic and tectonic events at ca 2.05 Ga ([37] by SHRIMP U–Pb/Zr) and may be therefore interpreted as a proximal area characterized by reworking and recycling of adjacent Archean cratonic crust [35].

### 3 Analytical techniques

#### 3.1 Mineral chemistry

Six (06) polished thin sections of the meta-mafic rocks from the Lolodorf region were examined in detail under the polarizing microscope to identify the mineral assemblages. The observed mineral assemblages were imaged and mineral compositions measured using a JOEL JXA 8230 electron microprobe at the Advanced Facility for Microscopy and Microanalysis (AFMM) of the Indian Institute of Science in Bangalore, India. Analytical conditions used were 15 kv, with 12 nA sample current and a beam width of 3  $\mu$ m. Count times for the major elements were 10 s on peaks and 5 s on each background. Natural silicate

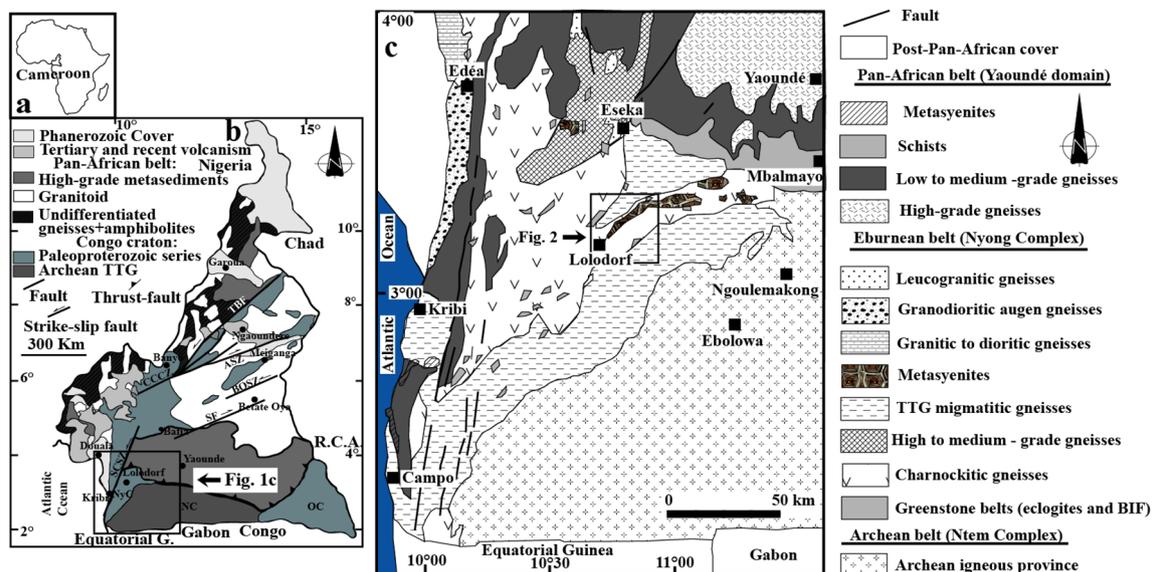


**Fig. 1** **a** Map of Cameroon in central Africa; **b** Geological sketch map of Cameroon modified after [33]; **c** Geological sketch map of the south-western Cameroon modified after [37]

**Table 1** Pressure and temperature results estimated on the studied samples

	Grt-Cpx [56]									
	Garnet					Clinopyroxene				
	XCa	XFe	XMg	XFe	XMg	XFe	XMg	Kd	Inferred T (°C)	P = 10.00 kbar
MO 31	0.175–0.209	0.537–0.583	0.275–0.313	0.250–0.281	0.585–0.656	4.747–6.641	697.00–821.00 °C	n = 7	766.00 °C	Retrogression
MO 33	0.175–0.187	0.597–0.629	0.214–0.249	0.292–0.320	0.572–0.628	5.560–7.090	687.00–749.00 °C	n = 21	710.00 °C	Retrogression
MO 47	0.210–0.280	0.453–0.502	0.343–0.364	0.200–0.210	0.606–0.694	5.160–6.580	729.00–856.00 °C	n = 7	805.00 °C	Peak temperature
MO 57	0.275–0.327	0.451–0.486	0.294–0.374	0.156–0.224	0.479–0.643	4.943–8.477	748.00–904.00 °C	n = 16	835.00 °C	Peak temperature
	Grt-Hbt [59] not pressure									
	Garnet					Amphibole				
	XCa	XFe	XMg	XFe	XMg	Kd	Inferred T (°C)			
MO 31	0.178–0.202	0.557–0.595	0.254–0.297	0.314–0.339	0.295–0.326	2.242–2.860	780.00–952.00 °C	n = 6	862.00 °C	Peak temperature
MO 33	0.180–0.186	0.607–0.619	0.222–0.244	0.279–0.322	0.352–0.413	4.173–5.188	708.00–866.00 °C	n = 6	784.00 °C	Retrogression
MO 47	0.211–0.279	0.449–0.502	0.343–0.364	0.239–0.257	0.390–0.420	2.821–3.323	760.00–889.00 °C	n = 7	828.00 °C	Peak temperature
MO 57	0.292–0.286	0.460–0.486	0.296–0.359	0.249–0.271	0.365–0.440	2.663–3.808	738.00–909.00 °C	n = 10	795.00 °C	Retrogression
	Grt-Pl-Hbl [60]									
	Garnet					Plagioclase Amphibole				
	XCa	XFe	XMg	XAn	XMg	Kd	Inferred P (kbar)			
MO 31	0.157–0.202	0.557–0.690	0.133–0.297	0.299–0.489	0.00–0.209	3.049–16.876	(T = 782.00 °C)	n = 6	9.70kbar	Décompression
MO 33	0.186–0.187	0.619–0.622	0.222–0.225	0.283–0.299	0.00–0.024	5.45–36.69	7.50–13.20kbr	n = 6	13.40kbar	Peak pressure
MO 47	0.253–0.822	0.174–0.474	0.007–0.358	0.696–0.990	0.029–0.077	4.872–507.07	13.20–14.90kbr	n = 9	9.10kbr	Décompression
							(T = 845.00 °C)			



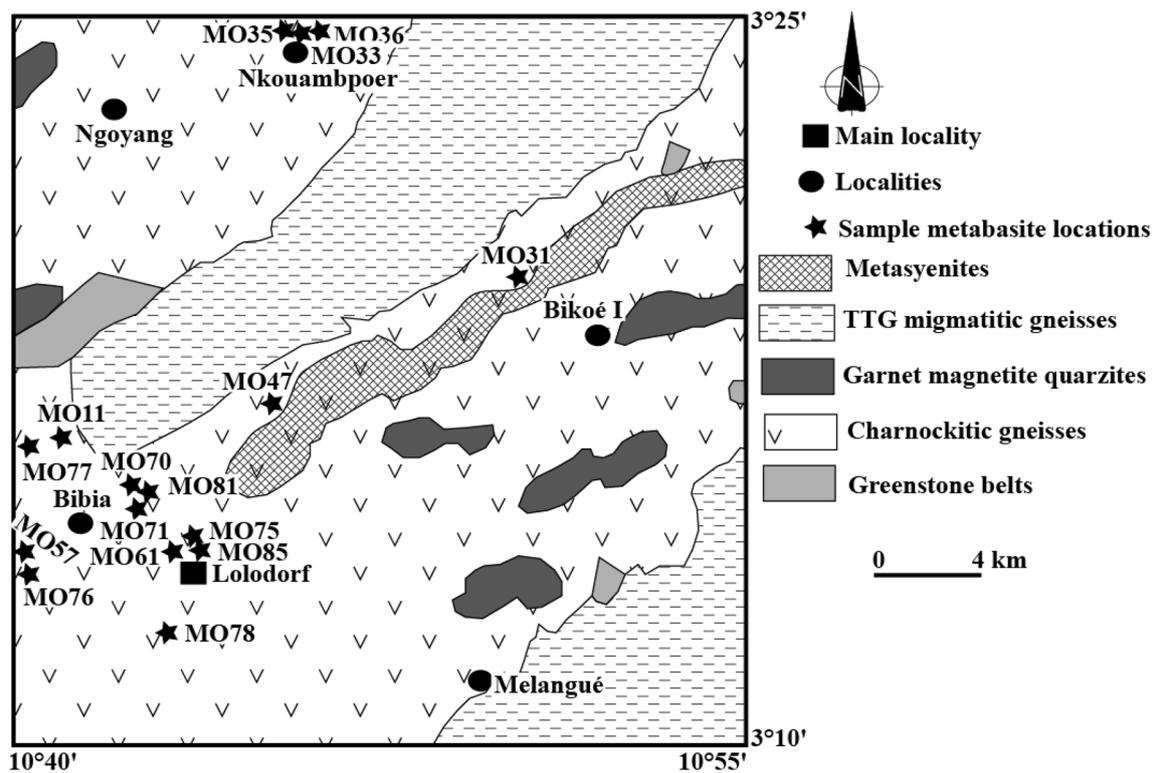


Fig. 2 Schematic map of the studied area modified after [20, 21, 37]. (Sample locations are represented by star)

and oxide minerals were used for calibration. Data were processed with a ZAF-type correction.

### 3.2 Whole rock geochemistry

Geochemical analysis of 14 samples was done using Inductively Coupled Plasma-Atomic Emission (ICP-AE) for major elements and Inductively Coupled Plasma Mass Spectrometry (ICP-MS) for trace elements including REE at the ALS Mineral Global Group, Vancouver (Canada). Sample preparation, analytical conditions and limits of detection are detailed in [52]. Major oxides and CIPW Norms are listed in Table 1, while trace elements and REE compositions are presented in Table 3. The CIPW norms were obtained using Excel spreadsheet program rewritten by [53].

## 4 Results

### 4.1 Petrography

Meta-mafic rocks of the Lolodorf area occur as enclaves within charnockitic gneisses (Fig. 2). They are represented by small bodies (Fig. 3a); plugs (15 to 20 m, Fig. 3d); dykes/

sills (~ 100–200 m length and 2–8 m width) and small lenses. They are melanocratic, fine to coarsed-grained and locally bear steep and flat foliations (Fig. 3a and c). At the mesoscale, they display in places, alternation of dark mafic and white felsic layers (Fig. 3a-c) or banding structures. The grain size distribution and melt segregation allow to classify into fine-grained garnet bearing meta-mafic (FGM) and coarse-grained garnet bearing meta-mafic (CGM) rocks (Fig. 3d, e).

The meta-mafics rocks display melt segregation (Fig. 3b, c) where quartz-plagioclasic phases are associated locally with garnet, amphibole and pyroxene. Locally, tiny leucosome pockets occur within the residual phase (Fig. 3).

They are mainly composed of garnet, clinopyroxene and amphibole (Fig. 3). Minor quartz and plagioclase are also observed in the hand-specimen. At the microscopic scale, the CGM display a granoblastic texture with heterogranular tendency (Fig. 4a, b) and granoporphyroblastic texture (Fig. 4c, d). They are mainly made up of garnet, clinopyroxene, amphibole, plagioclase, quartz, ilmenite, magnetite, apatite and rutile. The mineral distributions show a compositional variation from leucosome to melanosome bands or pockets (Fig. 4a, b). The leucosome is mainly composed of quartz-plagioclase aggregates,

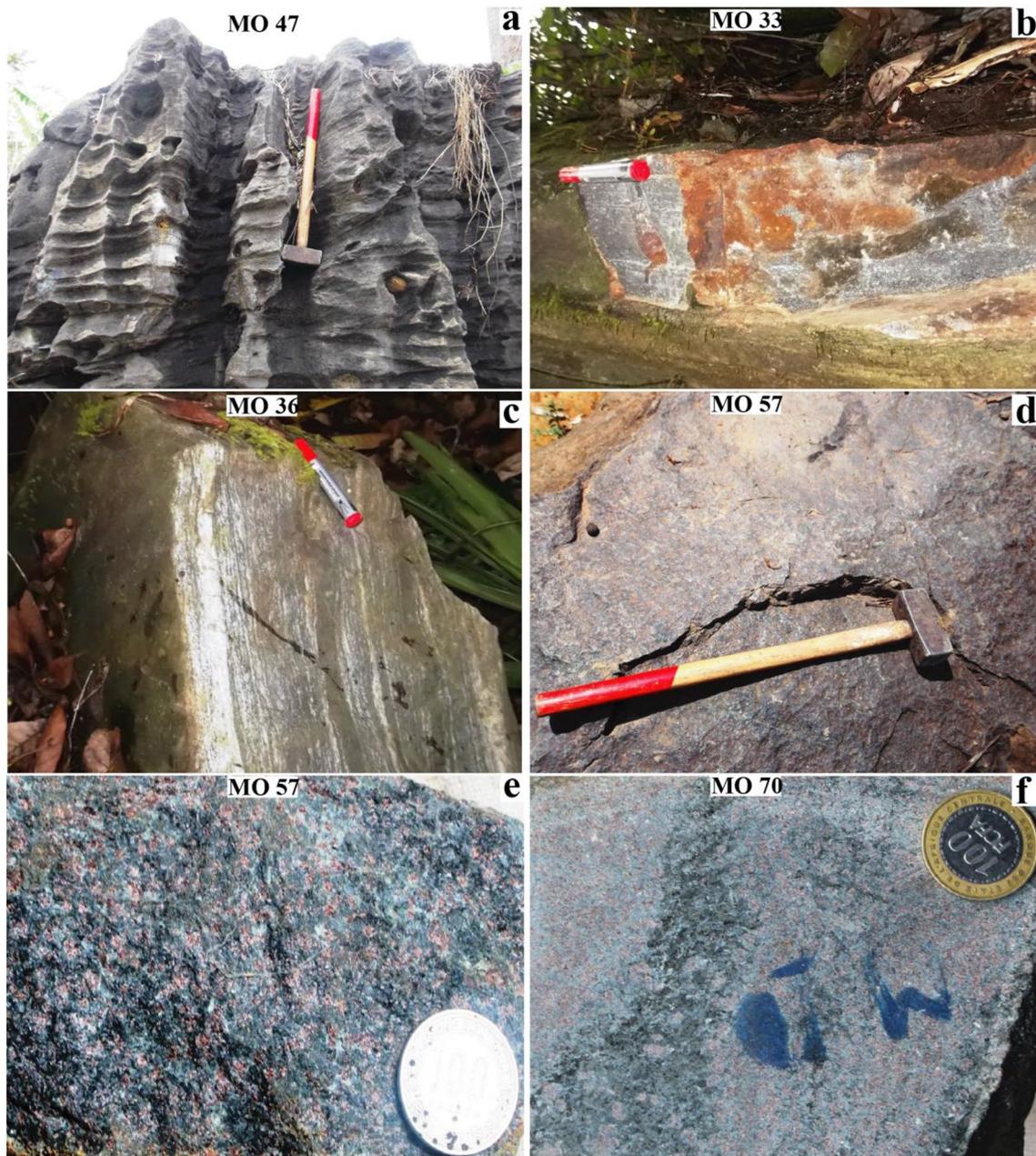


**Fig. 3** Field photographs of the studied granulite rocks. **a** Eroded meta-mafic rocks outcrop displaying flat foliation, **b** Massive meta-mafic rock plug, **c** Meta-mafic rocks sample at the mesoscale showing alternating mafic and felsic layers **d** Meta-mafic rocks outcrop

displaying steep foliation, **e** Hand-specimen of meta-mafic rocks displaying discontinuous tiny leucosome layers and leucosome pocket, **f** meta-mafic rocks displaying phenocrysts of garnet and clinopyroxene

sometimes crosscut by transgranular fracture filled with quartz monocrystals (Fig. 4b, c). Clusters of fine garnet and orthopyroxene (Fig. 4c, d) are often present in the quartz-plagioclase aggregates. The melanosome phase consists of subhedral garnet phenocrysts (Fig. 4d,

e and g, h), orthopyroxene, amphibole (Fig. 4e, f) and clinopyroxene, in places fractured (Fig. 4e). Ilmenite and magnetite are more abundant only within the residual phase (Figs. 2, 4a). Inclusions of garnet, quartz and plagioclase are present in the garnet and clinopyroxene

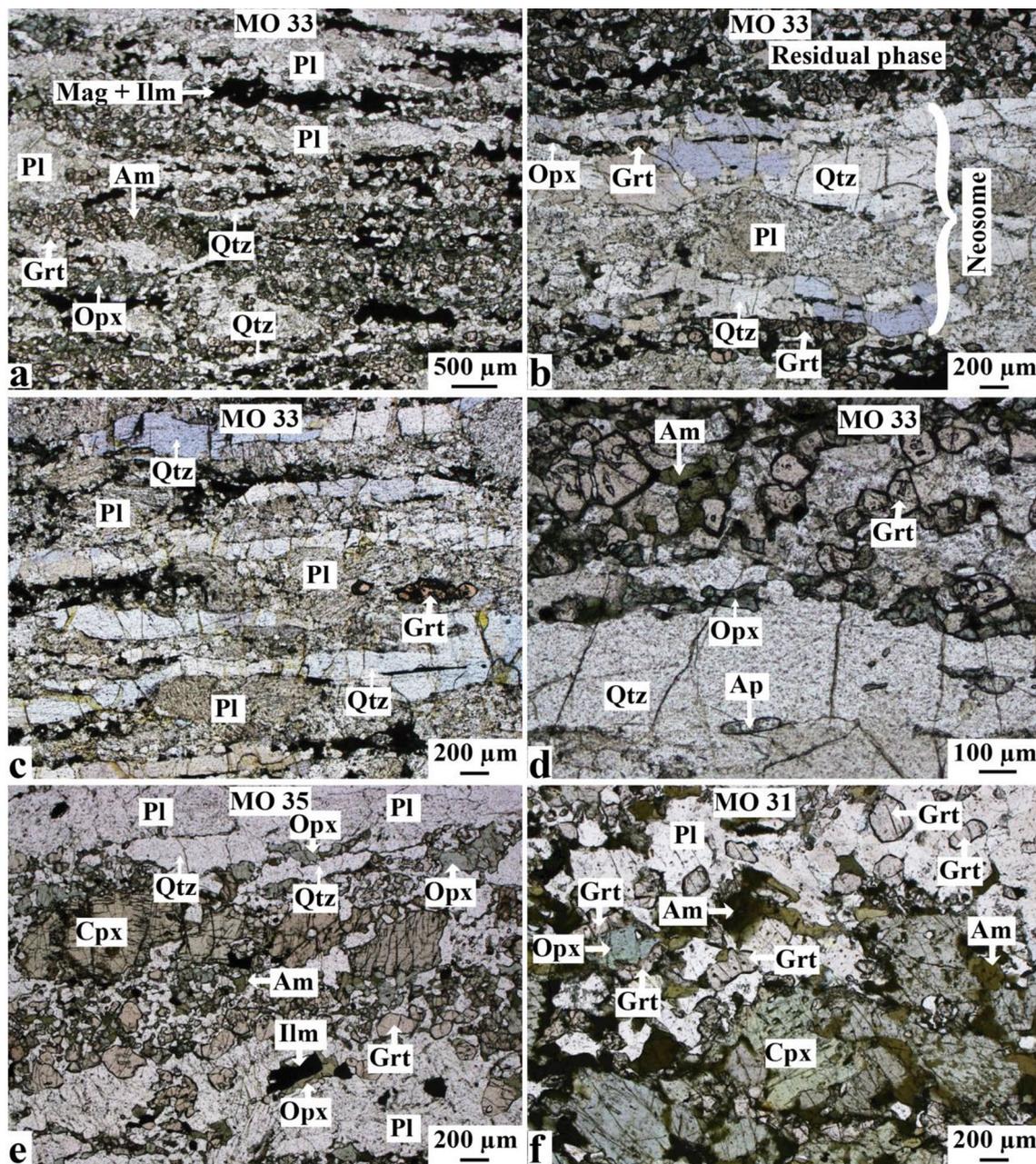


**Fig. 4** Microphotographs of the studied meta-mafic rocks. **a** Alternation of leucocratic layer of quartz (Qtz) ribbon and plagioclase (Pl) with mafic layer of pyroxene (Px) and garnet (Grt) necklace displaying both ductile deformation and partial melting features, **b** Melt segregation marked by alternation of neosome and residual phase bands, **c** Neosome phase displaying quartz (Qtz) ribbon, plagioclase (Pl) and garnet(Grt), **d** Coalesce garnet (Grt) displaying broken “necklace” around plagioclase (Pl) probably due to partial melting. Note the presence of amphibole (Am), and orthopyroxene (Opx) in the boundary between residual phase and neosome, **e** Tiny residual phase mainly made of ferromagnesian minerals. Note also tiny orthopyroxene (Opx) corona around

ilmenite (Ilm), **f** Green amphibole (Am) exsolution in clinopyroxene (Cpx), garnet (Grt) minerals dropped in the leucosome band, **g** Green amphibole (Am) between garnet (Grt) and clinopyroxene (Cpx). Note the presence of clinopyroxene (Cpx) and orthopyroxene (Opx) pseudomorphs and rutile (Ru), **h** Plagioclase(Pl), garnet (Grt), clinopyroxene (Cpx) and quartz (Qtz) assemblage. Note both exsolution and corona of green amphibole (Am) within clinopyroxene (Cpx), garnet (Grt) and clinopyroxene (Cpx) faces. **i** Partial corona of amphibole (Am) developed around (Cpx), **j** Equilibrium phase of amphibole (Am), garnet (Grt), clinopyroxene (Cpx), plagioclase (Pl) and quartz (Qtz), note also orthopyroxene (Opx) pseudomorph

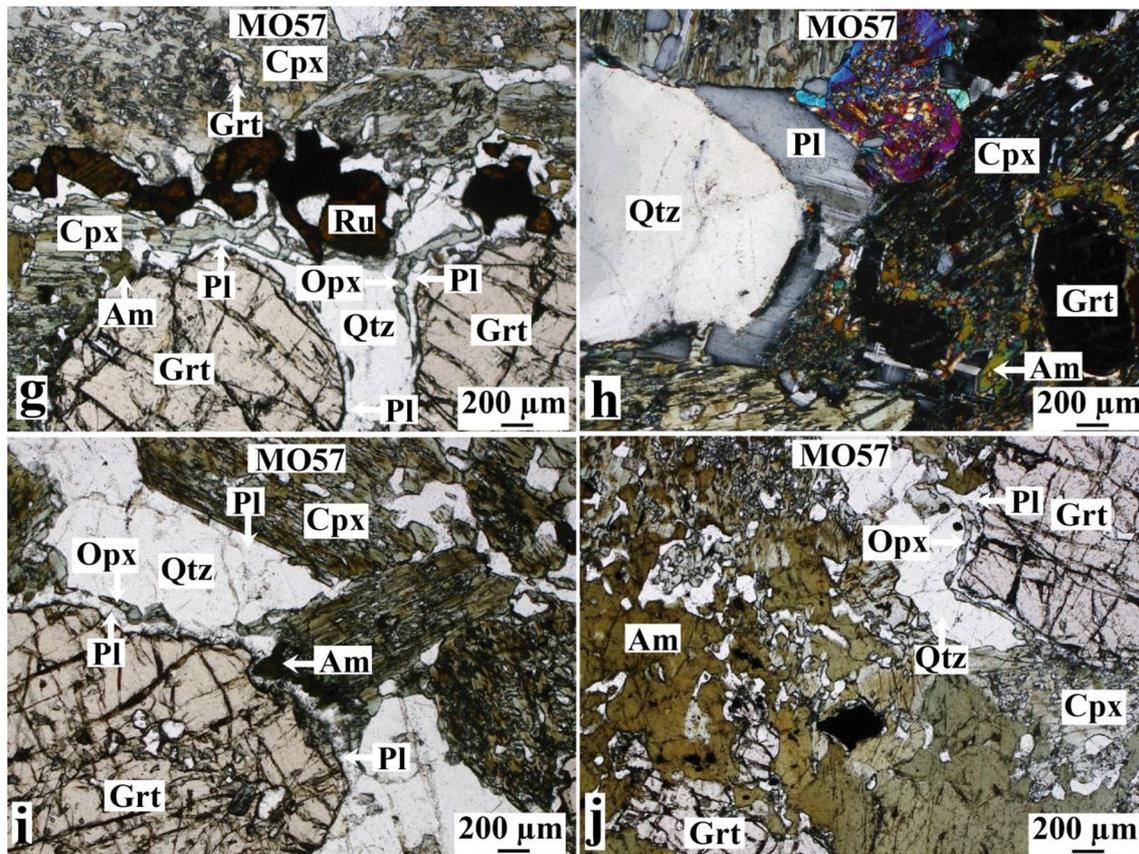


Fig. 4 (continued)

cores (Fig. 4g–i). In place garnet crystals are drowned in quartzoplagioclasic matrix (Fig. 4f). Some garnets are surrounded by reactionary rim. They are also associated with amphibole (Fig. 4f) and clinopyroxenes (Fig. 4i, j). Broken garnet necklaces are also found around the plagioclase (Fig. 4e, f) and display fractures filled with quartzfeldspathic phase which seals the two entities (Fig. 4k). Clinopyroxene is surrounded by corona of green amphibole (Fig. 4f, h, i) and displays straight boundary near the plagioclase crystal faces (Fig. 4h, i). Amphiboles are represented by brown–red and green types. Brown–red amphibole consists of large crystal grain up to 2 mm long, strongly pleochroic and showing in places quartz and plagioclase inclusions. Green amphibole also appears both as lamellae exsolution and as a rim around orthopyroxene and clinopyroxene crystals (Fig. 4f–j). Plagioclase occurs as subhedral to anhedral crystal in the matrix along with quartz and garnet (Fig. 4f). The orthopyroxene–plagioclase symplectite occurs between quartz and garnet crystals (Fig. 4g, i, j).

## 4.2 Mineral chemistry

Garnet, clinopyroxenes, orthopyroxenes, amphiboles and plagioclases are the analyzed mineral phases in this study. Garnet contains 17–63 mol% almandine, 17–82 mol% grossular, 0–27 mol% pyrope and 0–0.05 mol% spessartine with  $X_{Mg}$  number ranging from 0 to 0.36 (Supplementary file). Clinopyroxene contains 29.57–97.02 mol% wollastonite, 0–42.20 mol% enstatite and 2.98–19.31 mol% ferrosilite. In the binary Q–J diagram, all pyroxenes plot in the quad field (Fig. 5a). Clinopyroxenes are mainly diopsidic in nature and are locally augite and wollastonite. Primary diopside and Augite are  $Al_2O_3$  rich in their cores and decrease rimward from 8.69 to 1.73 for diopside and from 8.07 to 2.33 wt% for augite. They display 0.00 to 18.90 mol% jadeite with high values in the core. Orthopyroxene is clinoenstatite (Fig. 5b) with 0.85 mol% wollastonite, 52.94 mol% enstatite and 46.21 mol% ferrosilite (Supplementary file).

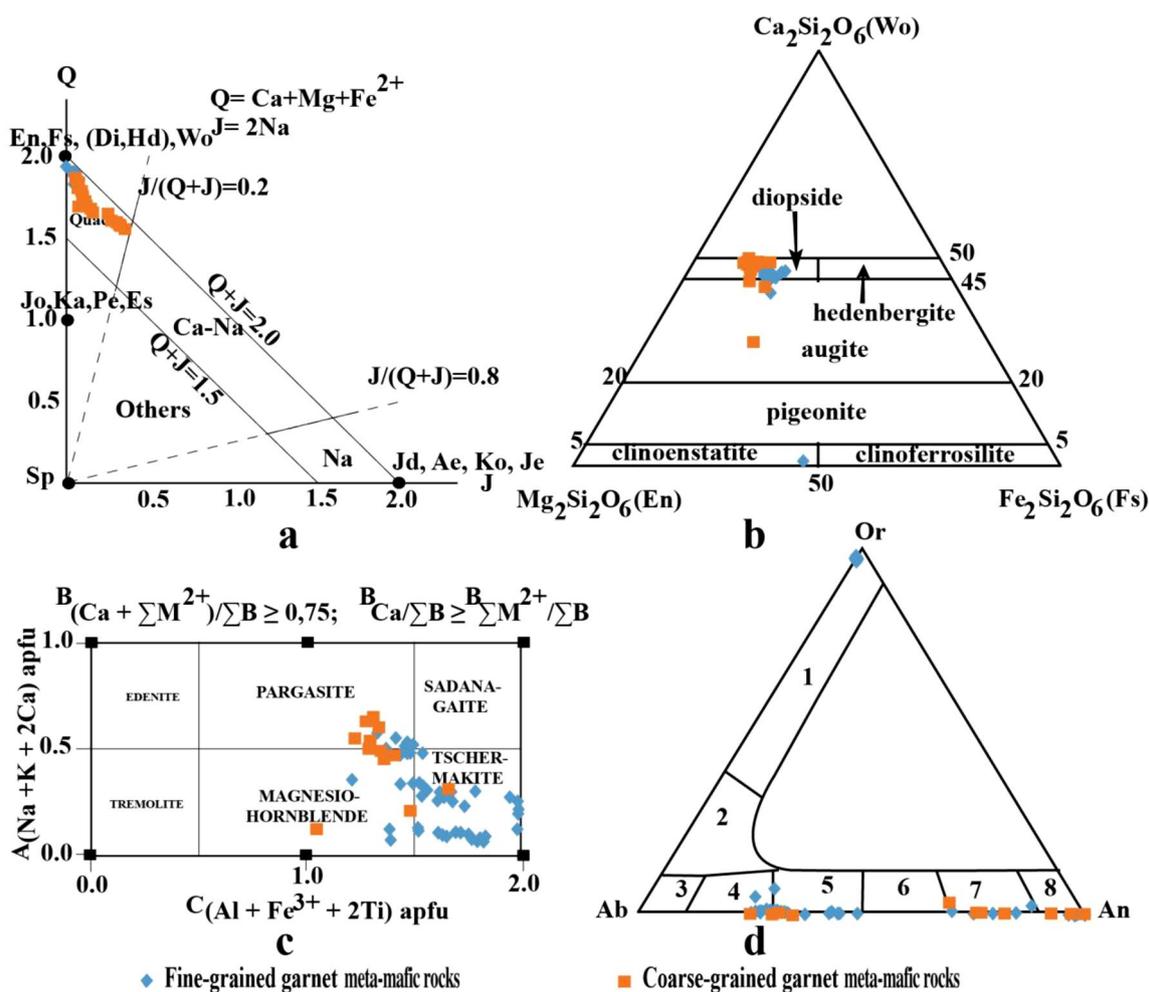


Fig. 5 **a** Q-J diagram showing studied sample plotting within the quad field, **b** Ternary diagram (En-Wo-Fs) for pyroxene classification [55], **c** Amphibole classification of studied samples [54], **d** Ab-Or-An ternary diagram of plagioclase classification

Amphiboles are calcic with Ca values ranging from 1.58 to 1.90 p.f.u., Na ranging from 0.19 and 0.78 p.f.u., and K values between 0.05 and 0.18 p.f.u. (Supplementary file). The primary amphiboles are Ti-rich with values ranging between 0.20 and 0.27 p.f.u., whereas the secondary amphiboles are Ti-poor (Ti = 0.03–0.18 p.f.u.). According to the classification of [54], these calcic amphiboles are represented by pargasite, magnesiohornblende and tschermakite end-members (Fig. 5c). The FGG (MO 33 and MO 47) samples are mainly composed of tschermakite and magnesiohornblende whereas the CGG (MO31 and MO 57) samples are composed of pargasite, magnesiohornblende and tschermakite (Fig. 5c).

Plagioclases contain 0.00–74.59 mol% albite, 25.17–100 mol% anorthite and 0.00–2.69 mol% orthoclase and consist of anorthite, bytownite, andesine and oligoclase end members (Fig. 5d). Anorthite contains

increase rimward from oligoclase to anorthite end members.

### 4.3 Thermobarometry, oxygen fugacity and water content estimates

The Grt-Cpx calibration of [56] is considered as the most accurate thermometer in the amphibolite-granulite-facies transition zone [57]. Using the Cpx-Grt assemblage, the thermometer yields average temperature of 766, 710 and 805 °C (Table 1) respectively for the MO 31, MO 33 and MO 47, all belonging to the FGM. The Hbl-Pl assemblage allows using equation from [58] that is based on edenite-tremolite reaction. According to this thermometer at high pressure condition of 10 kbar, the FGM (MO 31) sample displays temperatures ranging between 692 and 759 °C; with average temperature of 736 °C (Table 1).

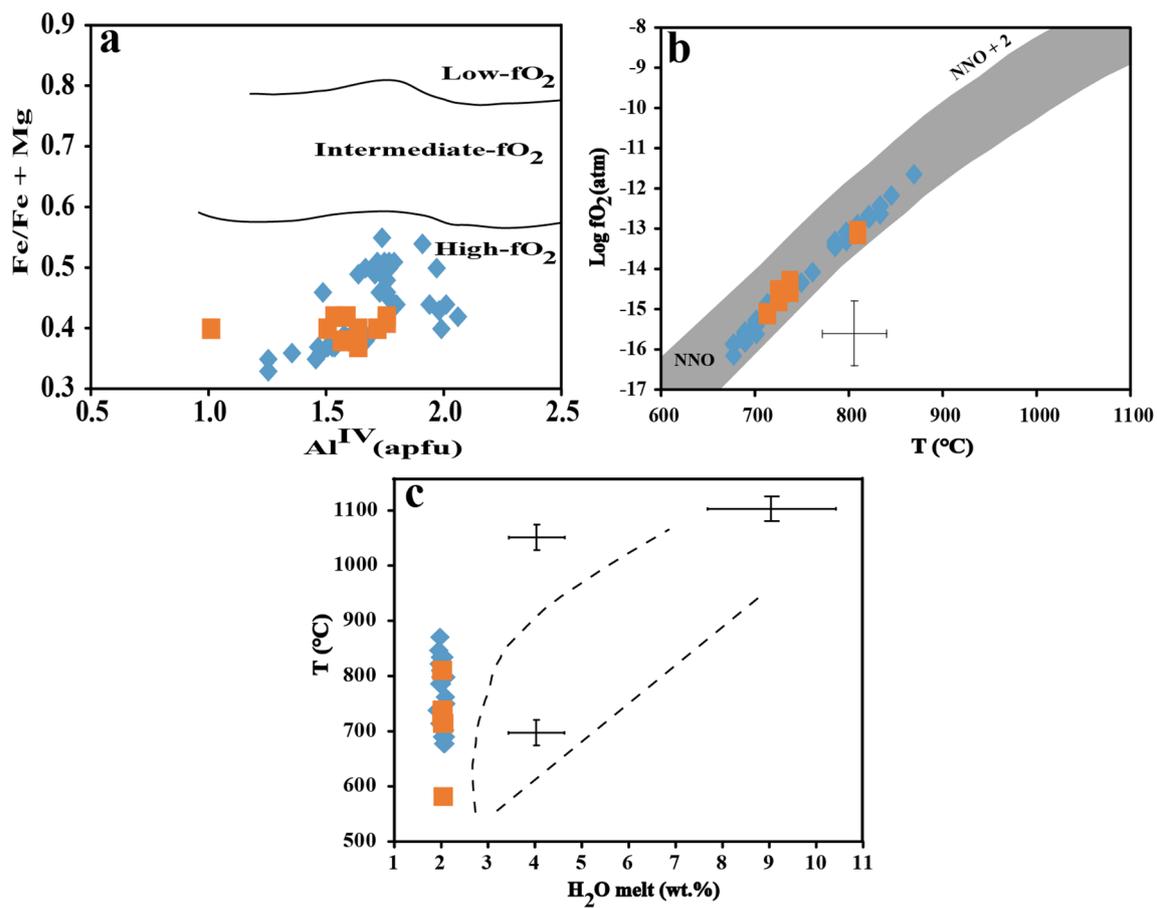


**Fig. 6** **a**  $\text{Al}^{\text{IV}}$  (apfu) vs.  $\text{Fe}/\text{Fe} + \text{Mg}$  diagram showing the compositional variation of amphiboles [64], **b**  $T$  ( $^{\circ}\text{C}$ ) vs.  $\log f(\text{O}_2)$  diagram of amphiboles after [62, 66]. The NNO and NNO+2 curves in (b) are taken from [67], **c**  $\text{H}_2\text{O}$  melt (wt%) vs.  $T$  ( $^{\circ}\text{C}$ ) diagram (after [66]). Error bars in (c) indicate the variation in accuracy with  $\text{H}_2\text{O}$  melt.

The maximum thermal stability (black dotted line at the left) and the lower limit (black dotted line at the right) of consistent amphiboles are also reported. For more explanations, see [66]. Symbols are the same as in Fig. 5

In the FGM (MO 33) sample, temperatures are ranged between 751 and 806  $^{\circ}\text{C}$ ; with an average temperature of 778  $^{\circ}\text{C}$  (Table 1). Considering low pressure condition of 5 kbar, temperatures are similar to those obtained during high pressure condition (10 kbar and in the CGM) whereas, in the FGM (MO 33), temperatures are higher in low pressure conditions than those obtained in the high pressure conditions (Table 1). As shown above, Grt-Hbl assemblage also has been used to calculate temperatures of anatectic melt. Calculation made using the calibration of [59] yielded a mean temperature estimate around 862, 784 and 828  $^{\circ}\text{C}$  in the FGM (MO 31, MO 33 and MO 47) samples respectively (Table 1). The barometer of [60] constrained in the FGM (MO 31, MO 33 and MO 47) samples yields a mean pressure estimate around 9.7, 13.4 and

9.1 kbar respectively (Table 1). Overall, the temperatures and pressures calculated above suggested P-T conditions of Cpx + Grt + Hbl + Pl range respectively between 9.1–13.4 kbar; and 710–862  $^{\circ}\text{C}$ . Such temperatures have widely varying oxygen fugacities (20.48–11.02 atm, pressures calculated after [61] in the equation of [62] ( $\log f\text{O}_2 = -30,930/T + 14.98 + 0.142(P - 1)/T$ ;  $T$  in  $^{\circ}\text{K}$  and  $P$  in bar (Supplementary file). Amphiboles are generally used as good proxy to understand the oxidation states of their host magma [63]. When plotted on the temperature versus  $\log f(\text{O}_2)$  diagram, the selected amphiboles from the present study fall in the NNO and NNO+2 buffers. The FGM crystallized between 11.69 and 15.92 atm and the CGM between 13.12 and 15.15 atm (Supplementary file, Fig. 6b). On the  $\text{Al}^{\text{IV}}$  versus  $\text{Fe}/\text{Fe} + \text{Mg}$  diagram (Fig. 6a) (stability

**Table 2** Major elements (wt%) and CIPW norm compositions of studied samples

Samples	MDL	Fine-grained garnet meta-mafic rocks								Coarse-grained garnet meta-mafic rocks					
		MO 31	MO 35	MO 47	MO 61	MO 75	MO 78	MO 81	MO 85	MO 11	MO 57	MO 70	MO 71	MO 76	MO 77
SiO <sub>2</sub>	0.01	48.67	50.70	48.60	48.20	49.01	49.55	48.39	50.15	46.68	46.69	49.23	49.70	50.27	48.54
TiO <sub>2</sub>	0.01	1.28	1.71	0.78	1.47	0.93	1.23	1.72	0.97	0.62	0.98	1.48	0.36	0.88	0.50
Al <sub>2</sub> O <sub>3</sub>	0.01	13.85	12.40	14.10	12.75	14.63	13.66	13.03	13.21	14.54	14.57	13.29	13.55	13.79	12.41
Cr <sub>2</sub> O <sub>3</sub>	0.00	0.03	0.02	0.05	0.03	0.00	0.03	0.03	0.04	0.06	0.03	0.03	0.03	0.06	0.13
Fe <sub>2</sub> O <sub>3</sub>	0.04	13.66	17.65	12.65	17.70	14.67	13.59	17.61	13.78	11.98	14.49	18.32	17.00	12.66	12.20
MnO	0.01	0.22	0.21	0.17	0.30	0.19	0.21	0.25	0.23	0.23	0.23	0.63	0.29	0.21	0.23
MgO	0.01	7.43	5.77	8.96	5.99	6.30	7.16	5.88	8.21	9.96	7.67	5.43	5.97	8.30	12.04
CaO	0.01	11.81	9.17	11.75	10.10	9.38	11.48	10.37	11.56	13.84	13.11	10.32	9.92	11.31	12.10
Na <sub>2</sub> O	0.01	2.22	2.22	1.65	2.18	3.42	2.08	2.08	1.60	1.36	1.80	1.53	2.07	2.00	1.24
K <sub>2</sub> O	0.01	0.28	0.48	0.12	0.23	0.63	0.38	0.29	0.05	0.07	0.10	0.17	0.22	0.29	0.15
P <sub>2</sub> O <sub>5</sub>	0.01	0.09	0.26	0.05	0.15	0.07	0.08	0.17	0.07	0.05	0.06	0.13	0.12	0.10	0.04
Loi	-5.10	0.20	-0.13	0.75	-0.02	0.50	0.30	-0.10	0.12	1.00	0.00	-0.80	0.09	0.13	0.41
Sum	0.01	99.74	100.46	99.63	99.08	99.73	99.75	99.72	99.99	100.39	99.73	99.76	99.32	100.00	99.99
Mg#		55.90	43.24	62.27	44.09	50.02	55.11	43.76	58.13	65.96	55.23	40.85	45.01	60.44	69.70
FeOt		12.29	15.88	11.38	15.93	13.20	12.23	15.85	12.40	10.78	13.04	16.48	15.30	11.39	10.98
K <sub>2</sub> O/Na <sub>2</sub> O		0.13	0.22	0.07	0.11	0.18	0.18	0.14	0.03	0.05	0.06	0.11	0.11	0.15	0.12

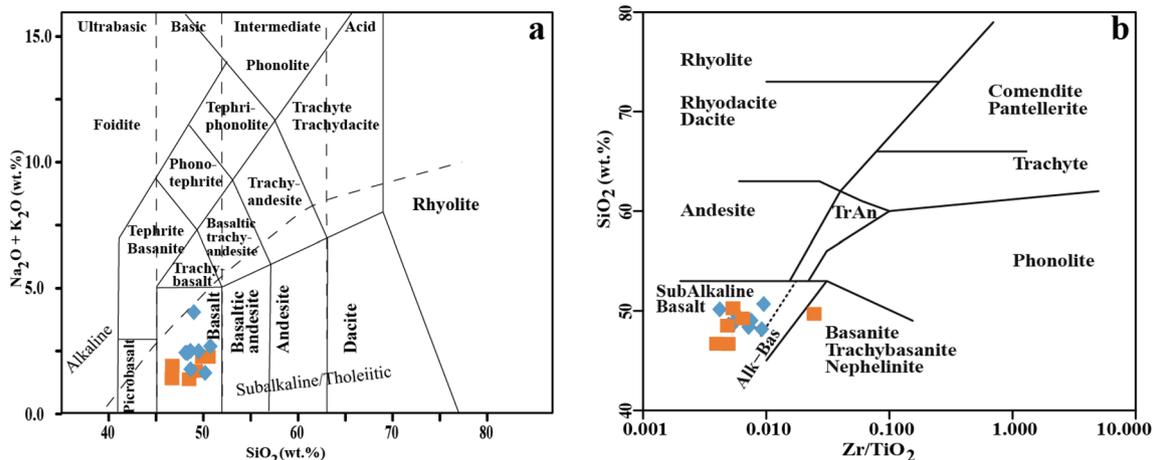


**Fig. 7** **a** Total alkali-Silica (TAS) diagram after [71] of the studied rocks and **b** Binary diagram from [70] showing the FGM and the CGM plotting in sub-alkaline basalts field. Symbols are the same as in Fig. 5

field after [64]), both the FGM and CGM show a high oxygen fugacity. [69] demonstrated that The Al<sup>VI</sup> content of amphiboles is sensitive to water content in the magma and then can be used for the estimation of the stability field of amphibole crystallization. Using the hygrometric formulation after [65] for the selected amphiboles, the calculation gave the value ranging from 1.92 to 2.10 wt% for the FGM and 2.02 to 2.06 wt% for the CGM (Fig. 6b, Supplementary file).

## 4.4 Whole rock geochemistry

### 4.4.1 Major elements

The major and trace element compositions of the studied granulites are reported on Table 2. The granulites display low SiO<sub>2</sub> (48.20–50.70 wt% for the FGM and 46.68–50.27 wt% for the CGM) and P<sub>2</sub>O<sub>5</sub> (0.05–0.26 wt% for the FGM and 0.04–0.13 wt% for the CGM) contents, high TiO<sub>2</sub>

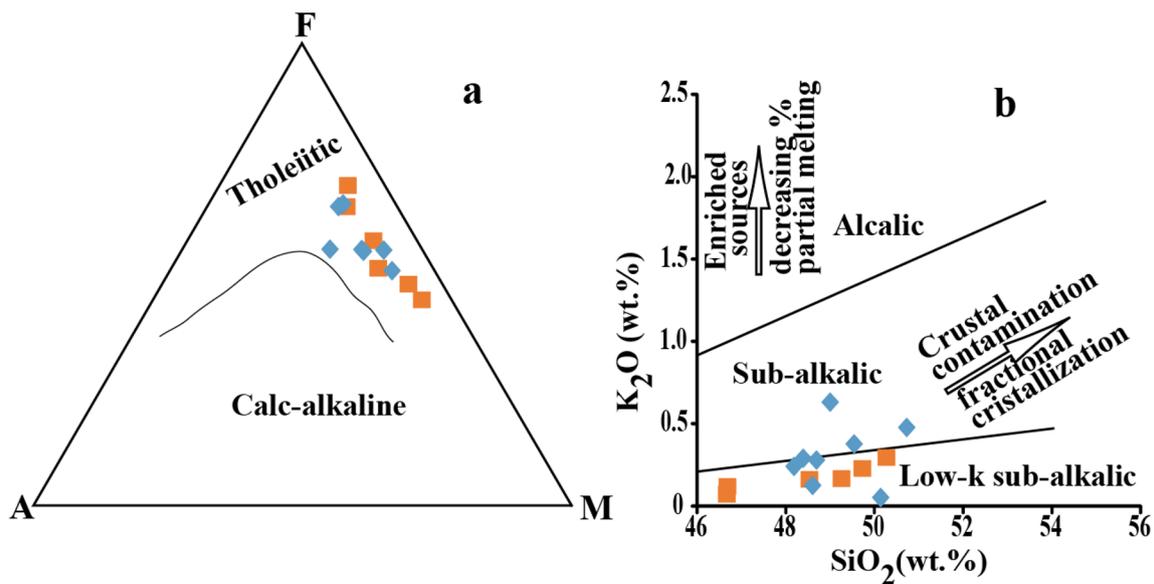


**Fig. 8** Nomenclature and classification diagrams of the studied meta-mafic rocks. **a** AFM ternary diagram (FeO+Na<sub>2</sub>O+K<sub>2</sub>O–MgO) after [68], and **b** binary diagram K<sub>2</sub>O vs. SiO<sub>2</sub> from [69]. Symbols are the same as in Fig. 5

(0.78–1.72 wt% for the FGM and 0.36–1.48 wt% for the CGM), CaO (9.17–11.81 wt% for the FGM and 9.72–13.84 wt% for the CGM), Fe<sub>2</sub>O<sub>3</sub> (12.65–17.65 wt% for the FGM and 11.98–18.32 wt% for the CGM) and MgO (5.77–8.96 wt% for the FGM and 5.43–12.04 wt% for the CGM) contents. Al<sub>2</sub>O<sub>3</sub> content shows a narrow range between 12.40 and 14.63 wt% for the FGM and 12.41 and 14.57 wt% for the CGM. The samples display a variable Mg number ( $Mg = 100 \times (MgO/40.31) / [(MgO/40.31) + ((Fe_2O_3 \times 0.8998) / 71.85 \times (1 - 0.15))]$ ) ranging from 43.24 to 62.27 of the FGM and 40.85 to 69.70 of the CGG (Table 2). The loss on ignition is low (LOI < 0.75 wt%), attesting to the freshness of the collected samples. Most of sample display high Na<sub>2</sub>O/K<sub>2</sub>O and Al<sub>2</sub>O<sub>3</sub>/TiO<sub>2</sub> ratios, 4.63–32 and 7.25–37.64 respectively. The FGM and the CGM are basaltic in composition as observed from their plots on the total alkali (Na<sub>2</sub>O+K<sub>2</sub>O) versus silica (SiO<sub>2</sub>) (TAS) diagram (Fig. 7a). Moreover, most of samples plot in the sub-alkaline basalt field on SiO<sub>2</sub> versus Zr/TiO<sub>2</sub> diagram of [70] (Fig. 7b), except for sample (MO71) which plots in the basanite field. The studied meta-mafic rocks plot exclusively in the tholeiitic field in the AFM ((Na<sub>2</sub>O–K<sub>2</sub>O)–FeO–MgO) ternary diagram (Fig. 8a, [68]). On the SiO<sub>2</sub> versus K<sub>2</sub>O diagram after [69], the studied samples plot in sub-alkalic and low-k sub-alkalic domain (Fig. 8b). On the Harker diagram of major oxides versus MgO, SiO<sub>2</sub>, Al<sub>2</sub>O<sub>3</sub>, K<sub>2</sub>O and MnO do not display any correlation with MgO while, Fe<sub>2</sub>O<sub>3</sub>, TiO<sub>2</sub>, Na<sub>2</sub>O and P<sub>2</sub>O<sub>5</sub> display a negative trend with increasing MgO while Cr<sub>2</sub>O<sub>3</sub> and CaO contents show a positive correlation with increasing MgO (Fig. 9).

#### 4.4.2 Trace elements

Trace and rare earth element concentrations are shown in the Table 3. The values of Cr are widely variable (23.71–360.00 ppm for the FGM and 230.00–1055.20 ppm for the CGM). Rb concentrations are generally low (0.66–14.60 ppm for the FGM and 1.40–4.70 ppm for the CGM). The Sr (67.10–232.8 ppm for the FGM and 21.80–72.00 ppm for the CGM) display a variable concentration, while Nb (1.60–11.70 ppm for the FGM and 1.10–4.60 ppm for the CGM) and Ta (0.10–0.70 ppm for the FGM and 0.10–0.35 ppm for the CGM) concentrations are low. On the bivariate plots (Fig. 10), Yb which is a relatively immobile trace element, display a strong positive correlations with Ho, Gd, Zr, and Y ( $R^2 > 0.80$ ), positive correlations with Nb, La, Sm, Ba ( $0.43 < R^2 < 0.68$ ) and no correlations with Rb ( $R^2 = 0.004$ ). The MgO display negative correlations with V, Zr, Nb, Y Hf and Ga (Fig. 11).

The chondrite-normalized REE spidergram [72] of the samples (Fig. 12c, d), show a nearly flat patterns with a little enrichment of the LREE compared to HREE. When plotted on the multi-element spidergram normalized to the primitive mantle [73] (Fig. 12a, b), the fine-grained garnet meta-mafic rocks exhibit relatively flat patterns with both positive and negative Ba and Sr anomalies while the coarse-grained garnet meta-mafic rocks show only Sr negative anomalies. The studied samples display Ce/Ce\* ratios ranging from 0.92 to 1.37 for the FGM and 0.81–3.10 ppm for the CGM, and slightly negative Eu

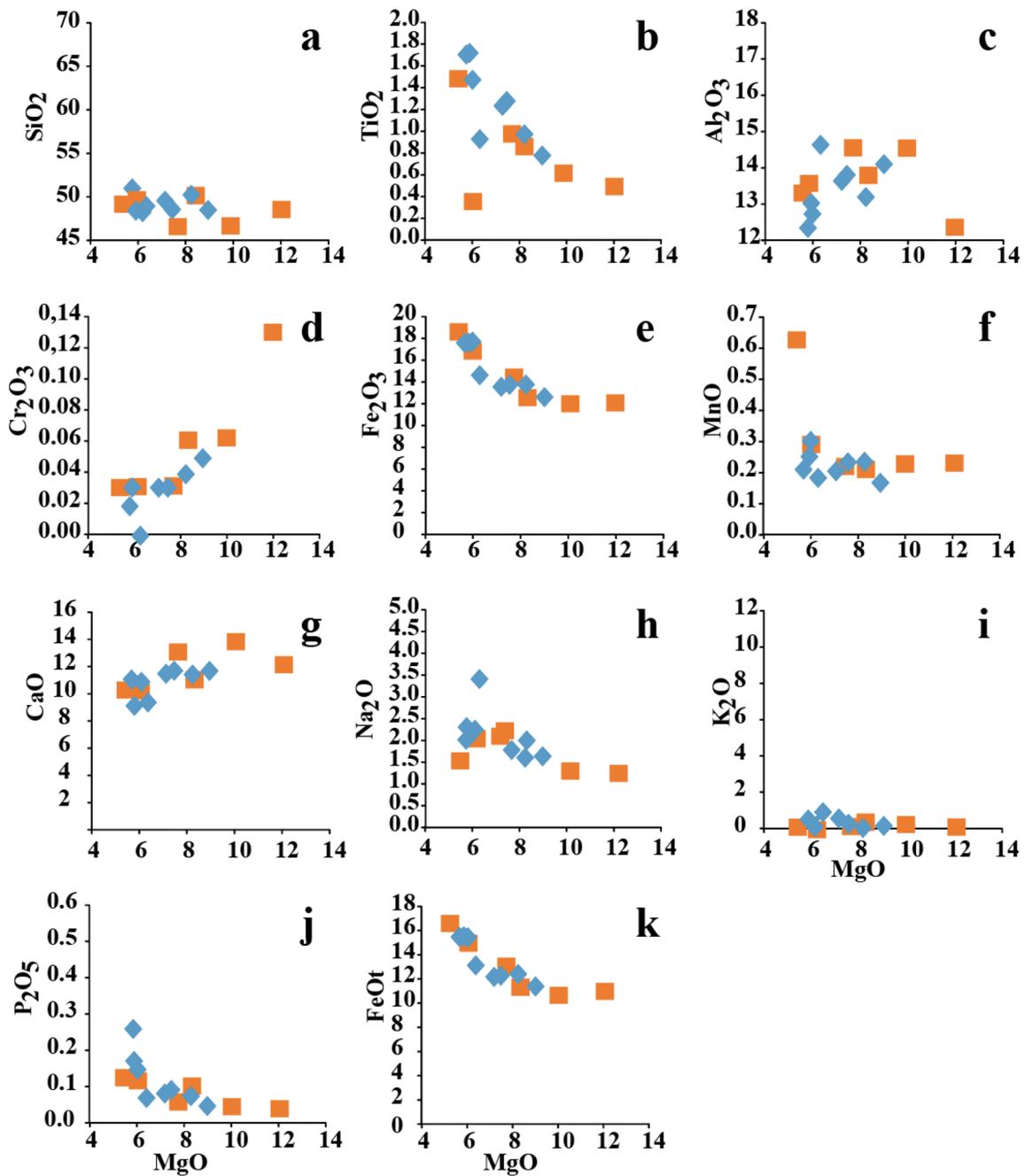


Fig. 9 Harker variation diagrams: MgO (wt%) versus major oxides (wt%). Symbols are the same as in Fig. 5

**Table 3** Traces elements (ppm) concentrations of studied samples

Samples	MDL	Fine-grained garnet meta-mafic rocks								Coarse-grained garnet meta-mafic rocks					
		MO 31	MO 35	MO 47	MO 61	MO 75	MO 78	MO 81	MO 85	MO 11	MO 57	MO 70	MO 71	MO 76	MO 77
<i>Trace elements (ppm)</i>															
Cr	8.00	221.31	140.00	360.00	240.00	23.71	213.41	252.93	329.82	495.32	252.93	268.74	230.00	443.32	1055.20
V	8.00	314.00	398.00	275.00	300.00	291.00	304.00	302.00	306.81	295.36	335.00	262.00	316.00	276.71	261.31
Rb	0.10	14.60	3.50	5.20	6.70	6.10	7.20	7.30	0.66	2.07	1.40	2.70	4.70	2.97	2.34
Sr	0.50	170.80	130.00	87.80	99.70	232.80	104.80	103.20	67.10	33.60	49.20	21.80	26.10	72.00	27.70
Y	0.10	20.80	67.30	15.30	41.90	20.00	21.30	46.70	20.60	17.39	23.90	41.00	31.50	22.90	16.10
Nb	0.10	5.00	11.70	1.60	4.80	6.00	4.20	5.30	2.60	1.70	2.40	4.60	3.30	4.50	1.10
Ba	1.00	75.00	286.00	56.90	97.50	128.00	39.00	99.00	4.49	27.55	23.00	20.00	35.60	97.42	11.81
Ga	0.50	16.60	21.00	15.10	18.70	19.90	18.10	18.00	15.81	13.03	14.80	14.70	19.40	15.08	11.29
Ta	0.10	0.20	0.70	0.10	0.30	0.40	0.20	0.40	–	–	0.10	0.30	0.20	0.35	–
Th	0.20	0.60	0.97	0.20	0.62	0.50	0.60	0.80	0.50	0.52	–	1.20	0.53	0.62	0.10
U	0.10	0.10	0.15	–	0.20	0.30	0.20	0.30	0.10	0.11	0.10	0.20	0.13	0.12	0.04
Zr	0.10	66.10	162.00	41.00	135.00	69.90	72.70	124.50	40.50	30.40	38.70	93.60	88.00	47.20	24.40
Hf	0.10	2.00	3.70	1.30	3.30	1.80	2.20	3.50	1.30	1.00	1.10	2.60	2.30	1.50	0.80
Sr/Y		8.21	1.93	5.74	2.38	11.64	4.92	2.21	3.26	1.93	2.06	0.53	0.83	3.14	1.72
<i>Rare-earth elements (ppm)</i>															
La	0.10	4.60	21.60	1.50	4.60	7.50	4.70	7.00	3.75	4.09	3.50	6.10	3.80	9.49	1.52
Ce	0.10	12.90	48.90	4.30	10.90	19.00	11.20	14.20	13.05	27.15	6.80	15.90	9.40	21.40	4.48
Pr	0.02	1.95	6.66	0.65	1.70	2.50	1.74	1.98	1.41	1.10	1.18	2.30	1.51	2.69	0.67
Nd	0.30	9.90	29.90	3.40	8.60	10.70	9.40	9.60	7.13	4.89	6.30	11.40	8.30	11.63	3.44
Sm	0.05	2.84	8.51	1.28	3.25	2.57	2.82	3.35	2.36	1.50	1.81	2.86	2.95	2.96	1.18
Eu	0.02	1.06	1.86	0.48	1.02	0.92	0.96	1.07	0.86	0.53	0.73	1.05	0.95	0.82	0.47
Gd	0.05	3.45	10.70	1.93	5.65	3.27	3.78	5.55	3.23	2.24	3.11	4.70	4.46	3.62	1.92
Tb	0.01	0.61	1.84	0.36	1.04	0.54	0.63	1.07	0.57	0.43	0.60	0.96	0.81	0.63	0.38
Dy	0.05	3.86	11.65	2.64	7.20	3.55	3.90	7.58	3.83	3.02	4.15	6.88	5.39	4.21	2.74
Ho	0.02	0.85	2.44	0.59	1.52	0.69	0.84	1.73	0.81	0.68	0.91	1.56	1.21	0.89	0.63
Er	0.03	2.18	7.02	1.82	4.72	2.24	2.25	5.32	2.36	2.10	2.82	4.94	3.47	2.70	1.91
Tm	0.01	0.30	1.05	0.30	0.68	0.31	0.32	0.77	0.34	0.32	0.40	0.68	0.53	0.40	0.28
Yb	0.05	2.01	6.59	1.88	4.35	1.97	2.00	4.83	2.28	2.11	2.65	4.37	3.70	2.64	1.86
Lu	0.01	0.32	0.98	0.27	0.66	0.30	0.31	0.73	0.35	0.32	0.38	0.68	0.52	0.42	0.29
TREE		46.83	159.70	21.40	55.89	56.06	44.85	64.78	42.33	50.48	35.34	64.38	47.00	64.50	21.77
Eu/Eu*		1.03	0.59	0.93	0.73	0.97	0.90	0.76	0.95	0.88	0.94	0.87	0.80	0.76	0.95
La <sub>N</sub> /Yb <sub>N</sub>		1.55	2.23	0.54	0.72	2.59	1.60	0.98	1.12	1.32	0.90	0.95	0.70	2.44	0.56
Ce <sub>N</sub> /Yb <sub>N</sub>		1.69	1.95	0.60	0.66	2.53	1.47	0.77	1.50	3.38	0.67	0.96	0.67	2.13	0.63

$$\text{Eu/Eu}^* = (\text{Eu}(\text{FGM}/\text{CFM})/\text{Eu}(\text{chon})) / (\text{Sm}(\text{FGM}/\text{CFM})/\text{Sm}(\text{chon}))^{1/2} (\text{Gd}(\text{FGM}/\text{CFM})/\text{Gd}(\text{chon}))^{1/2}$$

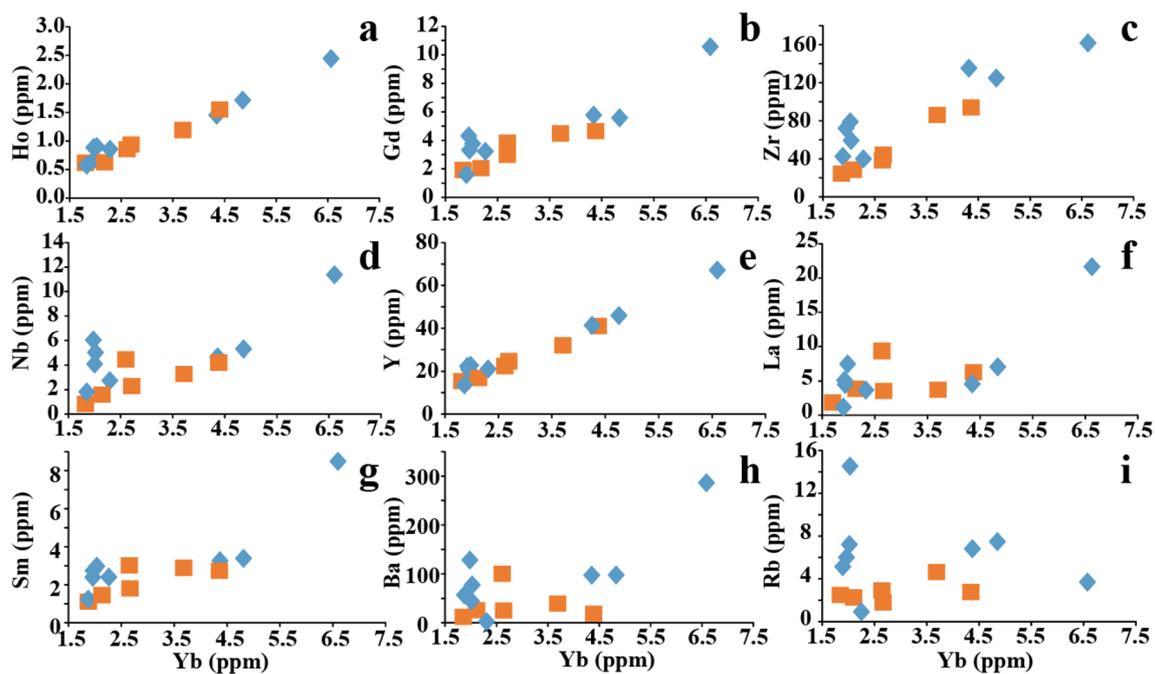


Fig. 10 Binary diagrams showing the trace element composition of the meta-mafic rocks samples. Symbols are the same as in Fig. 5

anomaly ( $\text{Eu}/\text{Eu}^* = 0.59\text{--}0.97$  for the FGM and  $0.76\text{--}0.95$  for the CGM).

## 5 Discussion

### 5.1 Petrographical evidence of anatexis melt and P–T conditions

The Lolodorf area and its surroundings display the meta-mafics rocks presenting partial melting evidences such as the presence of leucosome and melanosome at the mesoscopic scale (Fig. 3). On a microscopic scale, the presence of neosome and the residual phase (Fig. 4), significantly indicates the process of melt segregation [74]. Other evidences are the presence of quartzo-feldspathic beds hosting clinopyroxenes, orthopyroxenes and amphiboles; the dislocation of the garnet necklaces and the coalescence of the garnets in a broken chain scattered in the matrix (Fig. 4). The presence of aggregates of garnet and orthopyroxene in the neosome (Fig. 4), suggests grain migration, consistent with the presence of melt [75]. In addition, the reactive mineral aggregates in the residual phase and the quartz ribbon that cut the quartz-plagioclase aggregates in the neosome phase and the presence of the molten

edges of quartz and plagioclase along the grain boundaries further support this conclusion. The mineral recrystallization features on the studied rocks are also characterized by mantle and core microstructures and the neograins around the phenocrysts. All these microstructures occur at high temperature and are symptomatic of partial melting. The comparison of the studied meta-mafics rocks with migmatitic gneiss, TTG [37] and tonalitic gray gneiss where partial melting has been described in the NyC [47, 74] helps to reinforce the claim that the partial melting event was recorded on a regional scale.

The temperature and the pressure estimated by geothermobarometry are around  $672\text{--}952\text{ }^\circ\text{C}$ , and  $2.7\text{--}14.89$  kbar for the FGM and  $631\text{--}909\text{ }^\circ\text{C}$  and  $1.5\text{--}16.09$  kbar for the CGM. The mineral assemblage of the studied meta-mafics rocks was stable at higher oxygen fugacities ( $\text{LogO}_2$  varying from  $-15.67$  to  $-12.47$  atm for the FGM and  $-20.48$  to  $-12.67$  atm for the CGM). The above-mentioned metamorphic conditions of the studied meta-mafics rocks are nearly consistent with those from other mafic rocks from the Southwest Cameroon [20, 21, 76]. It is inferred that the amphibolite-granulite transition took place during a retrograde stage possibly related to a post-peak thermal overprint and/or fluid infiltration.

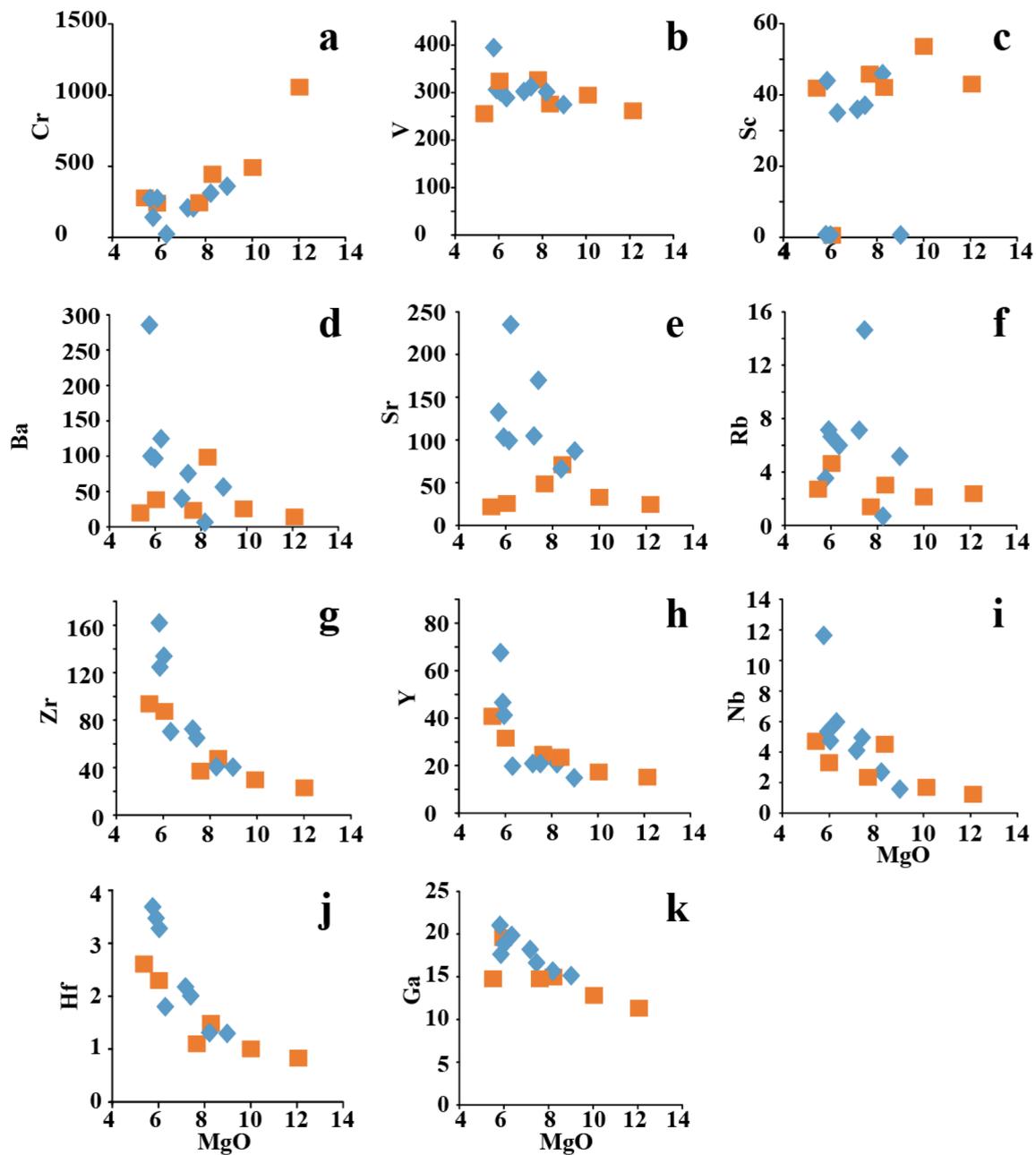


Fig. 11 Binary plots highlighting the HSFE relations with MgO. Symbols are the same as in Fig. 5

## 5.2 Origin and evolution of the granulites' protolith

The La/Th ratios are useful indicators of mafic or felsic source components, while Hf content generally reveals the degree of recycling. Hf (0.80–3.70 ppm) contents in

the studied meta-mafic rocks are very low suggesting the presence of intracratonic basin as it is the case in the previous works in the neighbouring NC [77]. The studied meta-mafic rocks display a wide range of La/Th ratios (0.00–22.27) that can be divided into two groups: below

**Fig. 12** **a** Chondrite-normalized REE patterns of FGM after [73], **b** Chondrite-normalized REE patterns of the FGM after [73], **c** Primitive mantle normalized multi-element spider diagram for the studied CGM after [72], **d** Primitive mantle normalized multi-element spider diagram for the studied CCM [72]. Symbols are the same as in Fig. 5

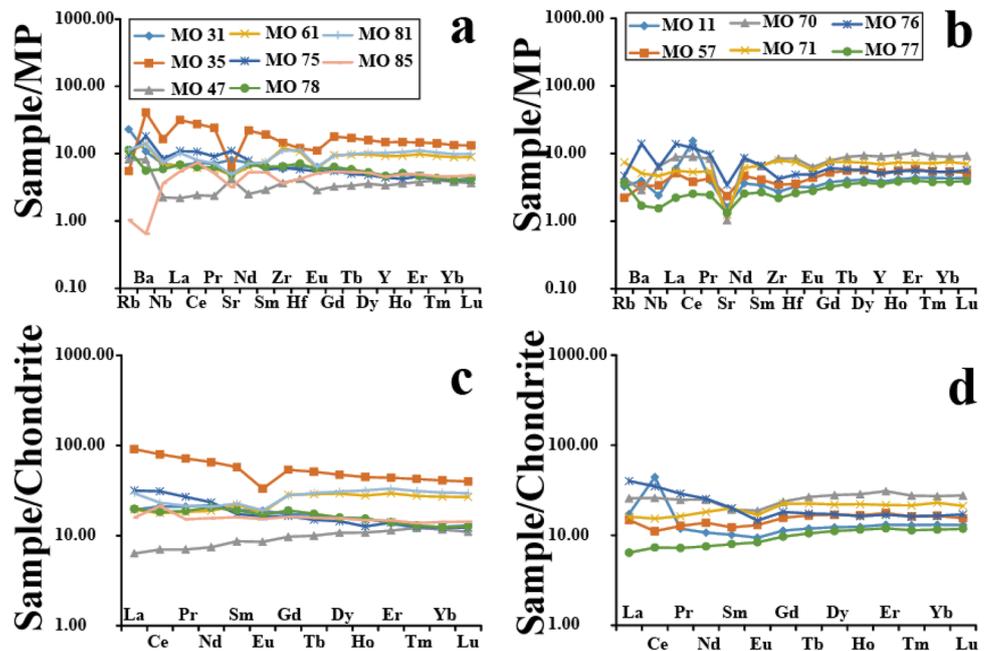
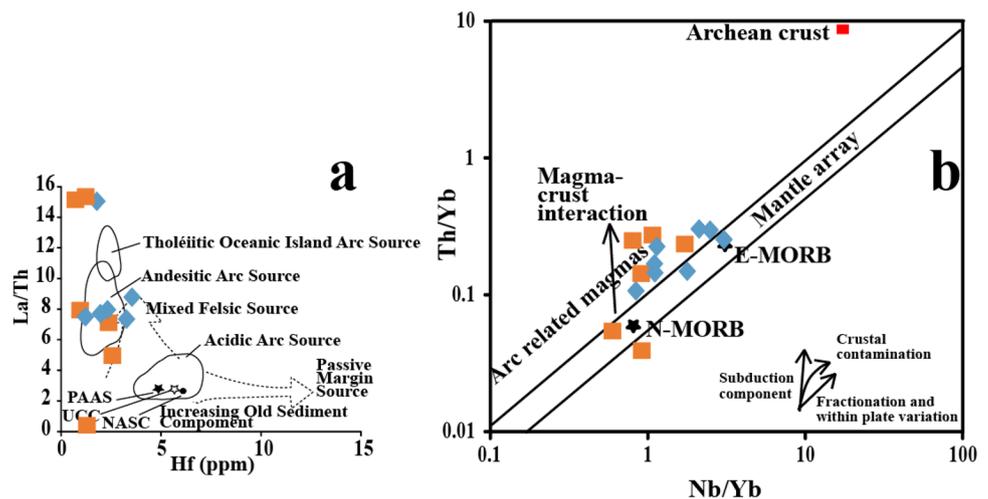


**Fig. 13** **a** Binary diagram of La/Th vs. Hf showing the rock sources, **b** Th/Yb vs. Nb/Yb diagram (after [2, 90]) showing the plots of the majority of the meta-mafic rocks falling in the arc-related magmas area. Few samples fall in the field for N-MORB and E-MORB. Symbols are the same as in Fig. 5



and above of 15. The La/Th ratios below 15 suggest the input of crustal sources or the presence of the sedimentary basin while the ratios above 15 (obtained from three samples) indicate that the studied samples may probably have mantle connection. This is consistent with the high Mg# (40.85–69.70) and the low SiO<sub>2</sub> (46.68–50.70 wt%) contents of the studied samples indicating the basaltic nature of the meta-mafics rocks protolith.

Moreover, the studied samples display high Na<sub>2</sub>O and low K<sub>2</sub>O contents [78], which is indicative of the partial melting of mafic rocks from the lower part of thickened crust [79, 80]. On the binary La/Th versus Hf diagram [81], the samples display high La/Th ratios except the MO 57 sample (Fig. 13a), defining a trend which perhaps reflects affinities with evolved “mixed felsic-basic arc” and

“andesitic arc” sources. When plotted in the Th/Yb versus Nb/Yb diagram (Fig. 13b; [3]), few samples (2 samples FGM and 01 sample CGM) plot in the fields of N-MORB and E-MORB, while most of the samples are plotted above the mantle array precisely on the magmatic arc field following an oblique linear trend, indicating the influence of crustal contamination and the partial melting in their generation. These characteristics suggest a remobilization of the already crystallized mafic rocks (protolith) in the active continental margin context [82]. The trace elements ratios such as the Nb/Th and La/Nb are very useful for the discrimination of the origin of the magmas [72]. The La/Nb ratios of the samples are between 0.92 (< 1) and 2.41, (> 1.0), indicating both the participation of the crust and the mantle components in the generation of

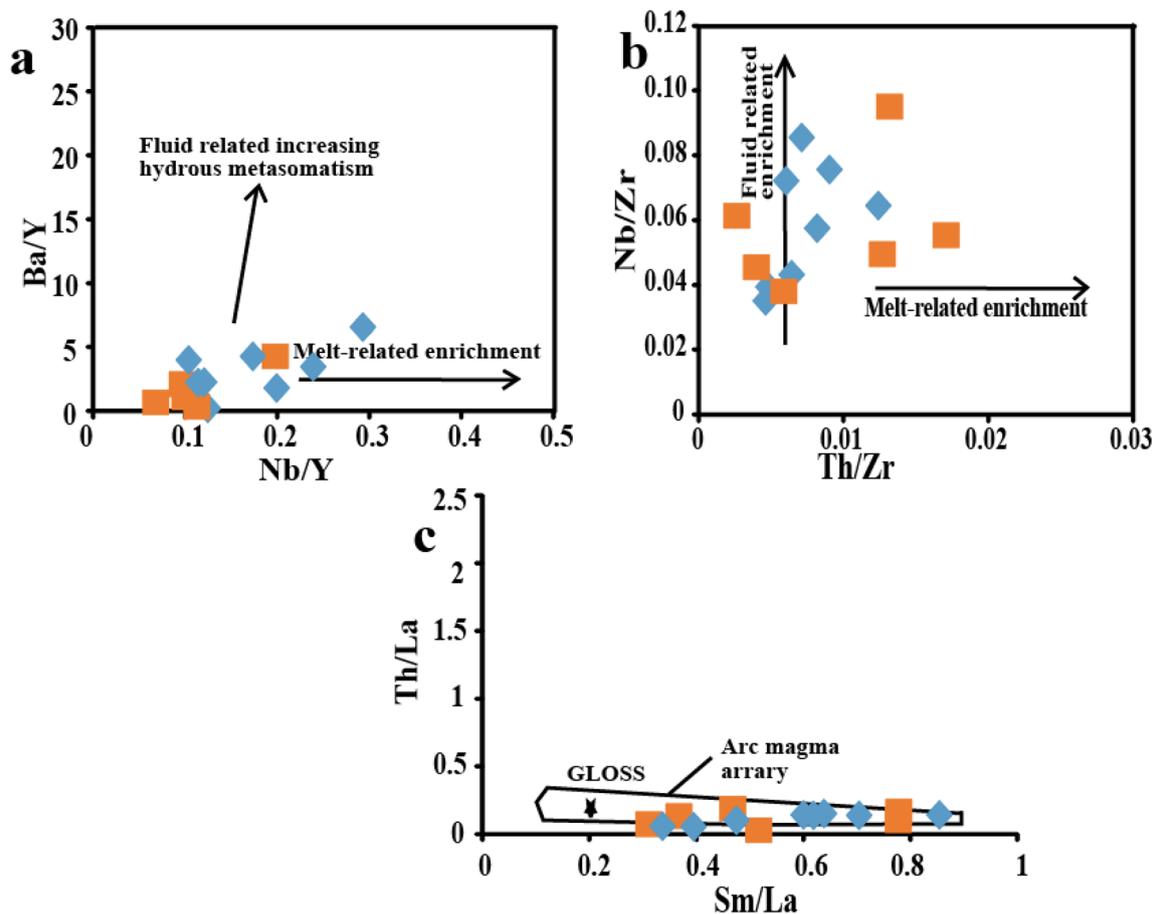


**Fig. 14** **a** Nb/Y vs. Ba/Y (after [85]), **b** Nb/Zr vs. Th/Zr (after [84]) for the studied meta-mafic rocks, **c** Sm/La vs. Th/La (after [91, 92]) showing the composition of the meta-mafic rocks. Symbols are the same as in Fig. 5

the Lolodorf mafics rocks. Such geochemical imprints are most often found in sub-alkaline, alkaline and tholeiitic formations [82]. The variable content of elements such as Ba (4.49–286.00 ppm), Sr (0.50–232.00 ppm), Zr (24.40–162.00 ppm) and Th (0.10–1.20 ppm) may indicate the fractionation of feldspars and zircon [83]. The enrichment of Rb, Ba, Th, K and La in some samples suggest the probable addition of components like sediments and fluids to the original mantle rock [84] prior to melting. In the Nb/Y versus Ba/Y (Fig. 14a) and Nb/Zr versus Th/Zr diagrams (Fig. 14b), the studied meta-mafics rocks define a trend indicating the mantle source modified by fluid phases and melt [84, 85]. In the Sm/La vs. Th/La diagram (Fig. 14c), all the studied samples are plotted in the arc magma array with few samples plotted very close to the global subducting sediment (GLOSS) [86], indicating the influence of melt during the evolution of these rocks.

These behaviors indicate the contribution of the continental crust and mantle to the generation of the studied rocks [87]. The  $K_2O/P_2O_5$  ratio (0.71 and 9) indicates a minimum to maximum involvement of the silicic component

of the crust. In general, the studied samples display  $Eu/Eu^* > 0.6$ , typical of source rocks affected by intracrustal differentiation processes [88]. Overall, a combination of these results suggests that the protolith of the studied rocks was mafic magma generated in an active continental margin (Fig. 13b). The presence of the melt segregation observed in macroscopic and microscopic scales suggests that the rocks may have been affected by high grade metamorphism associated with the migmatization or partial melting. Both the composition of the mantle source and the degree of partial melting that produced the parental magmas of the studied meta-mafic rocks can be determined using REE abundances and ratios. In the La/Sm vs. La diagram (Fig. 15a) the majority of the samples are plotted along the trend of partial melting and one sample along the fractional crystallization indicating the predominance high degree of partial melting during the generation of magma sources of these rocks. Moreover, the Sm versus Sm/Yb diagram after [89] point to the contribution of 4–68% melting of the spinel lherzolite source (Fig. 15b). Plotted on the Zr/4-2Nb-Y triangular diagram

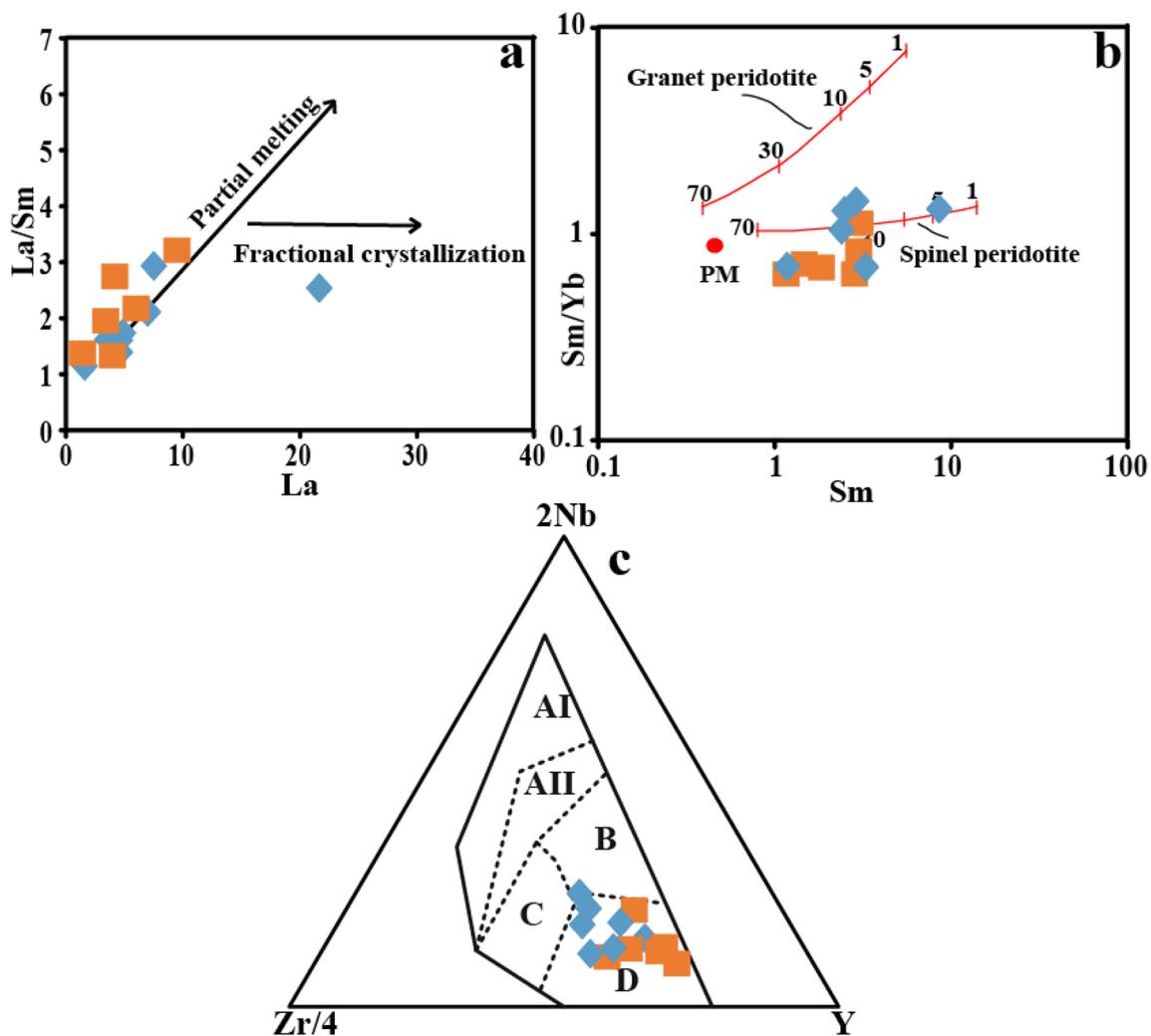


**Fig. 15** **a** The La vs. La/Sm diagram of the meta-mafic rocks indicating mostly partial melting during evolution of the rocks, **b** Sm/Yb vs. Sm plot (after [89]) showing the degree of partial melting of the

studied rocks and **c** Zr/4-2Nb-Y triangular diagram of [90] showing the meta-mafics plotting in the field of N-MORB. Symbols are the same as in Fig. 5

of [90] indicating the geotectonic contexts of the basalts (Fig. 15c), the studied meta-mafics of Lolodorf and its surroundings fall on the N-MORB field.

The results from the studied meta-mafics rocks from the Lolodorf area are consistent with recent studies on the NyC mafic rocks that point to a conclusion that the protolith of eclogite are basaltic in compositions, with tholeiitic nature and MORB affinities [20, 21].

### 5.3 Relative emplacement ages

The studied fine-grained meta-mafic rocks (FGM) display the petrographical, mineralogical and geochemical characteristics of samples that went through partial melting and metamorphism (MO31, MO33, MO36 and MO47) while the Coarse-grained meta-mafic rocks (CGM) display

only metamorphic signature (MO57). The FGM displays banded patterns while the second does not. The features highlighted on the CGM are similar to those of previous studies in the NyC (dated at ca. 2.09 Ga) [20]. Then, the 2.09 Ga obtained in the NyC rocks could be assigned to the CGM [20]. The FGM (banded samples) were emplaced before the partial melting even, probably during Mesoarchean period while the CCM may have crystallized during Eburnean period [35, 46, 49].

The amphibolite-granulite facies transition observed on the Lolodorf meta-mafic rocks have been also recorded in the mafic and charnockitic rocks from the NyC in Cameroon (2.05 Ga, [20, 46]), in the migmatitic gneiss of Ivory Cost (2.05- 2.03 Ga, [93–95]) and in Brazil (2.10–2.07 Ga, [96]). The restricted range of ages observed in high grade metamorphic rocks

(2.10–2.03 Ga, [20, 93–95, 97]) and within the mafic rocks (2.09 Ga, [20]) suggest that the partial melting and the metamorphism may belong to the same event developed during the Eburnean orogeny at relatively limited time span. Overall, Mesoarchean high pressure mafic rocks (FGM protoliths) may have been reworked [35, 46, 49] coeval to the emplacement of juvenile meta-mafic rocks (CGM) during Eburnean period. This assumption is supported by previous works stipulating that the NC (which is an Archean nucleus crust) has interacted with juvenile Eburnean crust as described in other orogens (Thompson belt, Canada; Terre Adélie, Antarctica; Finland; Man Rise, Ivory Coast; [3, 14, 98].

## 6 Conclusion

In this study, mineralogical, geochemical and petrographical results of the Lolodorf mafic rocks studied disclose the following conclusions:

The Lolodorf area is made up of fine-grained and coarse-grained garnet meta-mafic rocks presenting granoblastic to granoporphyroblastic texture. They consist of quartz, plagioclase, garnet, orthopyroxene, clinopyroxene, amphibole, opaques, apatite and rutile.

The petrological study of the selected samples indicates that partial melting and peak of metamorphism occur under conditions close to amphibolite-granulite transition. The fine-grained garnet meta-mafic rocks emplaced under pressure estimated at around 2.7–14.89 kbar with temperature interval between 672 and 952 °C while the coarse-grained garnet meta-mafic rocks settled at around 1.5–16.09 kbar and temperature between 631 and 909 °C. The studied samples crystallized under high oxidizing conditions with low water content. The Mesoarchean fine-grained meta-mafic rocks protolith may have experienced Eburnean partial melting and metamorphic processes whereas the coarse-grained garnet meta-mafic rocks would have experienced only metamorphic process during Eburnean orogeny.

The geodynamic implications of the studied meta-mafic rocks suggest that an Eburnean convergence has implemented reworking and emplacement of the juvenile magmatic crust under high pressure and high temperature (HP-HT) conditions favoring intense partial melting. These processes have implied a crustal thickening and subsequent rapid exhumation of the studied meta-mafic rocks.

**Acknowledgements** The authors are grateful to Professor Sajeew Krishnan from the Indian Institute of Science, Bagalore for facilitating mineral chemistry analyses. We would like to thank anonymous reviewers, whose helpful comments and suggestions improved the quality of this manuscript.

**Author contributions** All authors contributed to the study conception and design. Material preparation, data collection and analysis were performed by EJMO, SMN, BN, RCMT, SBB, FNB and JMO. The first draft of the manuscript was written by EJMO and all authors commented on previous versions of the manuscript. All authors read and approved the final manuscript.

**Funding** The authors declare that no funds, grants, or other support were received during the preparation of this manuscript.

**Data availability** The whole-rock geochemical (major and trace element) and mineralogical data used in this manuscript are original and reported in the tables.

## Declarations

**Conflict of interest** The authors declare that they have no known competing financial interests or personal relationships that could have appeared to influence the work reported in this paper.

**Open Access** This article is licensed under a Creative Commons Attribution 4.0 International License, which permits use, sharing, adaptation, distribution and reproduction in any medium or format, as long as you give appropriate credit to the original author(s) and the source, provide a link to the Creative Commons licence, and indicate if changes were made. The images or other third party material in this article are included in the article's Creative Commons licence, unless indicated otherwise in a credit line to the material. If material is not included in the article's Creative Commons licence and your intended use is not permitted by statutory regulation or exceeds the permitted use, you will need to obtain permission directly from the copyright holder. To view a copy of this licence, visit <http://creativecommons.org/licenses/by/4.0/>.

## References

1. Condie KC (2005) High field strength element ratios in Archean basalts: a window to evolving sources of mantle plumes? *Lithos* 79:491–504
2. Pearce JA (2008) Geochemical fingerprinting of oceanic basalts with applications to ophiolite classification and the search for Archean oceanic crust. *Lithos* 100:14–48
3. Pitra P, Kouamelan AN, Ballèvre M, Peucat JJ (2010) Palaeoproterozoic high-pressure granulite overprint of the Archean continental crust: evidence for homogeneous crustal thickening (Man Rise, Ivory Coast). *J Metamorph Geol* 28:41–58. <https://doi.org/10.1111/j.1525-1314.2009.00852.x>
4. Cook YA, Sanislav IV, Hammerli J, Blenkinsop TG, Dirks PHG (2016) A primitive mantle source for the Neoproterozoic mafic rocks from the Tanzania craton. *Geosci Front* 7:911–926
5. de Wit MJ, Hart RA, Hart RJ (1987) The Jamestown Ophiolite complex, Barberton Mountain Belt: a section through 3.5 Ga oceanic crust. *J Afr Earth Sci* 6(5):681–730
6. Bagas L, Kolb J, Fiorentini ML, Thebaud N, Owen J, Rennick S, Stensgaard BM (2016) On the processes that formed archaean Ni-Cu sulfide mineralisation in the deep continental crust, thrym complex, Southeastern Greenland. *Precamb Res* 277:68–86
7. Johnson TE, Brown M, Goodenough KM, Clark C, Kinny PD, White RW (2016) Subduction or sagduction? Ambiguity in constraining the origin of ultramafic-mafic bodies in the Archean crust of NW Scotland. *Precamb Res* 283:89–105

8. Szilas K, Van Hinsberg VJ, Creaser RA, Kisters AFMM, Hinsberg V, Van Kisters AFMM (2014) The geochemical composition of serpentinites in the MesoarchaeoanTartoq Group, SW Greenland: Harzburgitic cumulates or melt-modified mantle? *Lithos* 198–199(1):103–116
9. Szilas K, Van Hinsberg V, McDonald I, Næraa T, Rollinson H, Adetunji J, Bird D, Hinsberg V, Van McDonald I, Næraa T, Rollinson H, Adetunji J, Bird D (2018) Highly Refractory archaean peridotite cumulates: petrology and geochemistry of the Seqi Ultramafic complex, SW Greenland. *Geosci Front* 9(3):689–714
10. Vidal M, Delor C, Pouclet A, Siméon Y, Alric G (1996) Evolution géodynamique de l'Afrique de l'Ouest entre 2,2 Ga et 2 Ga: le style "archéen" des ceintures vertes et des ensembles sédimentaires birimiens du nord-est de la Côte-d'Ivoire. *Bull Soc Géol Fr* 167(3):307–319
11. Cagnard F, Gapais D, Barbey P (2007) Collision tectonics involving juvenile crust: the example of the southern Finnish Svecofennides. *Precamb Res* 154:125–141
12. McLaren S, Sandiford M, Powell R (2005) Contrasting styles of Proterozoic crustal evolution: a hot-plate tectonic model for Australian terranes. *Geology* 33:673–676
13. Cagnard F, Brun J-P, Gapais D (2006) Modes of thickening of analogue weak lithospheres. *Tectonophysics* 421:145–160
14. Gapais D, Pelletier A, Ménot R-P, Peucat JJ (2008) Paleoproterozoic tectonics in the Terre Adélie Craton (East Antarctica). *Precamb Res* 162(3–4):531–539
15. Möller A, Appel P, Mezger K, Schenk V (1995) Evidence for a 2 Ga subduction zone: eclogites in the Usagaran belt of Tanzania. *Geology* 23:1067–1070
16. Collins AS, Reddy SM, Buchan C, Mruma A (2004) Temporal constraints on Palaeoproterozoic eclogite formation and exhumation (Usagaran Orogen, Tanzania). *Earth Planet Sci Lett* 224:175–192
17. Pearce JA, Cann JR (1973) Tectonic setting of basic volcanic rocks determined using trace element analyses. *Earth Planet Sci Lett* 19:290–300
18. Wang D, Guo J, Huang G, Scheltens M (2015) The Neoproterozoic Ultramafic-Mafic complex in the Yinshan block, North China Craton: magmatic monitor of development of archaic lithospheric mantle. *Precamb Res* 270:80–99
19. Guo R, Liu S, Bai X, Wang W (2017) A Neoproterozoic Subduction recorded by the Eastern Hebei Precambrian Basement, North China Craton: geochemical fingerprints from Metavolcanic Rocks of the Saheqiao-Shangying-Qinglong Supracrustal Belt. *J Asian Earth Sci* 135:347–369
20. Loose D, Schenk V (2018) 2.09 Ga old eclogites in the eburnean-transamazonian orogeny of southern Cameroon: Significance for Paleoproterozoic plate tectonics. *Precamb Res* 304:1–11
21. Houketchang Bouyo M, Penaye J, Mouri H, Toteu SF (2019) Eclogite facies metabasites from the Paleoproterozoic Nyong Group, SW Cameroon: mineralogical evidence and implications for a high-pressure metamorphism related to a subduction zone at the NW margin of the Archean Congo craton. *J Afr Earth Sc* 149:215–234
22. Nga Essomba TP, Ganno S, Tanko NE, Ndema MJ, Kamguia WB, Soh TL, Takoudjou WJ, Nzenti JP (2020) Geochemical constraints on the origin and tectonic setting of the serpentinized peridotites from the Paleoproterozoic Nyongderies, Eseka area SW Cameroon. *Acta Geochim* 39:404–422
23. Smith MP, Henderson P, Campbell LS (2000) Fractionation of the REE during hydrothermal processes: constraints from the Bayan Obo Fe-REE-Nb Deposit, Inner Mongolia, China. *Geochim Cosmochim Acta* 64(18):3141–3160
24. Rolland Y, Cox S, Boullier A, Pennacchioni G, Mancktelow N (2003) Rare earth and trace element mobility in mid-crustal shear zones: insights from the Mont Blanc Massif (Western Alps). *Earth Planet Sci Lett* 214:203–219
25. Powell W, Zhang M, Reilly SYO, Tiepolo M (2004) Mantle amphibole trace element and isotopic signatures trace multiple metasomatic episodes in Lithospheric Mantle, Western Victoria, Australia. *Lithos* 75:141–171
26. Štípská P, Schulmann K, Kröner A (2004) Vertical extrusion and middle crustal spreading of omphacite granulite: a model of syn-convergent exhumation (Bohemian Massif, Czech Republic). *J Metamorph Geol* 22:179–198
27. Schulmann K, Lexa O, Štípská P, Racek M, Tajčmanová L, Konopásek J, Edel JB, Peschler A, Lehmann J (2008) Vertical extrusion and horizontal channel flow of orogenic lower crust: key exhumation mechanisms in large hot orogens? *J Metamorph Geol* 26:273–297
28. Pearce JA (2014) Geochemical fingerprinting of the earth's oldest rocks. *Geology* 42(2):175–176
29. Arndt N (1999) Why was flood volcanism on submerged continental platforms so common in the Precambrian? *Precamb Res* 97(3–4):155–164
30. Castaing C, Feybesse JL, Thieblemont D, Triboulet C, Chevremont P (1994) Paleogeographical reconstructions of the Pan-African/Brasiliano orogen: closure of an oceanic domain or intracontinental convergence between major blocks. *Precamb Res* 69:327–344
31. Trompette R (1994) Geology of western Gondwana (2000–500 Ma) Pan-African-Braziliano aggregation of South America and Africa. Rotterdam, A.A Balkema, p 350
32. de Wit MJ, Stankiewicz J, Reeves C (2008) Restoring Pan-African-Brasiliano connections: more Gondwana control, less Trans-Atlantic corruption. In: Pankurst RJ, Trouw RAJ, Brito Neves BB, de Wit MJ (eds) *West Gondwana pre-cenozoic correlations across the South Atlantic region*, vol 294. Geological Society London Special Publications, London, pp 399–412
33. Owona S, Mvondo Ondo J, Ratschbacher L, Mbola Ndzana SP, Tchoua MF, Ekdeck GE (2011) The geometry of the Archean, Paleoproterozoic tectonics in the Southwest Cameroon. *Comptes Rendus Geosci* 343:312–322
34. Feybesse JL, Johan V, Triboulet C, Guerrot C, Mayaga-Mikolo F, Bouchet V, Eko N'dong J (1998) The West Central African Belt: a model of 2.5–2.0 Ga accretion and two-phase orogenic evolution. *Precamb Res* 87:161–216
35. Penaye J, Toteu SF, Tchameni R, Van Schmus WR, Tchakounté J, Ganwa AA, Minyem D, Nsifa EN (2004) The 2.1 Ga West Central African Belt in Cameroon: extension and evolution. *J Afr Earth Sci* 39:159–164
36. Neves SP, Bruguier O, Vaucher A, Bosch D, Rangel Da Silva JM, Mariano G (2006) Timing of crust formation, deposition of supracrustal sequences, and Transamazonian and Brasiliano metamorphism in the East Pernambuco belt (Borborema Province NE Brazil): implications for western Gondwana assembly. *Precamb Res* 149:197–216
37. Lerouge C, Cocherie A, Toteu SF, Penaye J, Milesi JP, Tchameni R, Nsifa NE, Fanning CM, Deloule E (2006) SHRIMP U/Pb zircon age evidence for paleoproterozoic sedimentation and 2.05 Ga syntectonic plutonism in the Nyong Group, South-western Cameroon: consequences for the eburnean-transamazonian belt of NE Brazil and central Africa. *J Afr Earth Sc* 44:413–427
38. Boniface N, Schenk V, Appel P (2012) Paleoproterozoic eclogites of MORB-type chemistry and three. Proterozoic orogenic cycles in the Ubendian Belt (Tanzania): evidence from monazite and zircon geochronology, and geochemistry. *Precamb Res* 192–195:16–33
39. Ntomba SM, Ndong BF, Messi OEJ, Goussi NFJ, Bisso D, Magnekou TCR, Mvondo OJ (2016) Phlogopite compositions as indicator of both the geodynamic context of granitoids and the

- metallogeology aspect in Memvé/éle Archean area, north western Congo Craton. *J Afr Earth Sc* 118:231–244
40. Maurizot P, Abessolo A, Feybesse JL, Johan LP (1986) Etude de prospection minière du Sud-Ouest Cameroun. Synthèse des travaux de 1978 à 1985. Rapport BRGM 85:274p
  41. Vicat J-P, Moloto-A-Kenguemba G, Pouclet A (2001) Les granitoïdes de la couverture protérozoïque de la bordure nord du craton du Congo (Sud-Est du Cameroun et Sud-Ouest de la République centrafricaine), témoins d'une activité magmatique post-kibarienne à pré-panafricaine. *Compte Rendu de l'Académie des Sciences. Paris, Sciences de la Terre et des Planètes/ Earth and Planetary Sciences* 332:235–242
  42. Ganwa AA, Klötzli US, Hauzenberger C (2016) Evidence for Archean inheritance in the pre-Panafrican crust of Central Cameroon: insight from zircon internal structure and LA-MC-ICP-MS U-Pb ages. *J Afr Earth Sc* 120:12–22
  43. Tchakounté Numbem J, Toteu SF, Van Schmus WR, Pénaye J, Deloule E, MvondoOndoua J, Houketchang Bouyo M, Ganwa AA, White WM (2007) Evidence of ca. 1.6-Ga detrital Zircon in the Bafia Group (Cameroon): implication for the chronostratigraphy of the Pan-African Belt north of the Congo craton. *Comptes Rendus de l'Académie des Sciences* 339:132–142
  44. Tchakounté J, Eglinger A, Toteu SF, Zeh A, Nkoumbou C, MvondoOndoua J, Pénaye J, De Wit M, Barbey P (2017) The Adamawa-Yadé domain, a piece of Archean crust in the Neoproterozoic Central Orogenic belt (Bafia area, Cameroon). *Precamb Res* 299:210–229
  45. Van Schmus WR, Toteu SF (1992) Where the Congo craton and the São Francisco craton joined during the fusion of Gondwanaland? *EOJ Abstr* 7:25
  46. Toteu SF, Van Schmus WR, Pénaye J, Nyobe JB (1994) U-Pb and Sm–Nd evidence for Eburnean and Pan-African high grade metamorphism in cratonic rocks of Southern Cameroon. *Precamb Res* 67:321–347
  47. Nédélec A, Minyem D, Barbey P (1993) High P-High T anatexis of archean tonalitic grey gneisses: the Esékamigmatites, Cameroon. *Precamb Res* 62:191–205
  48. KamguiaWoguia B, DjibrilKouankapNono G, Nga EssombaT-soungui PE, TankoNjiosseu EL, AyontaKenne P, Nzenti JP (2022) Geochemistry and U-Pb zircon age of the Paleoproterozoic metasedimentary rocks from the Bidou I, Nyong Series, Cameroon: implications for provenance and tectonic setting. *Arab J Geosci* 15:154. <https://doi.org/10.1007/s12517-022-09476-7>
  49. Tchameni R, Mezger K, Nsifa EN, Pouclet A (2001) Crustal origin of Early Proterozoic syenites in the Congo Craton (Ntem Complex), South Cameroon. *Lithos* 57:23–42
  50. Pinghua L, Fulai L, Hong Y, Fang W, Jianhui L (2012) Protolith ages and timing of peak and retrograde metamorphism of the high-pressure granulites in the Shandong Peninsula, eastern North China Craton. *Geosci Front* 3(6):923–943
  51. Shoujie L, Bor-ming J, Yusheng W, Hangqiang X, Shijin W, Shiven X, Chunyan D, Mingzhu M, Dunyi L (2015) Neoproterozoic to Paleoproterozoic high-pressure mafic granulite from the Jiaodong Terrain, North China Craton: petrology, zircon age determination and geological implications. *Gondwana Res* 28:493–508
  52. Ganno S, Ngnotue T, Kouankap NGD, Nzenti JP, Notsa FM (2015) Petrology and geochemistry of the banded iron-formations from Ntem complex greenstones belt, Elom area, Southern Cameroon: implications for the origin and depositional environment. *Geochemistry* 75:375–387
  53. Kurt Hollocher (2014) Excel spreadsheet for CIPW calculation. Geology Department, Union College Schenectady, NY, 12308, [hollochk@union.edu](mailto:hollochk@union.edu)
  54. Hawthorne FCR, Oberti GE, Harlow WV, Maresch RF, Martin JC, Schumacher M, Welch D (2012) Nomenclature of the amphibole supergroup. *Am Miner* 97:2031–2048
  55. Morimoto N, Fabries J, Ferguson AK, Ginzburg IV, Ross M, Seifert FA, Zussman J, Aoki K, Gottardi G (1988) Nomenclature of pyroxenes. *Am Mineral* 73:1123–1133
  56. Ellis DJ, Green DH (1979) An experimental study of the effect of Ca upon the Grt-Cpx Fe-Mg exchange equilibria. *Contrib Mineral Petrol* 71:13–22
  57. Johnson CA, Bohlen SR, Essene EJ (1983) An evaluation of garnet-clinopyroxene geothermometry in granulites. *Contrib Mineral Petrol* 84:191–198
  58. Holland T, Blundy J (1994) Non ideal interactions in calcic-amphiboles and their bearing on amphibole-plagioclase thermometry. *Contrib Mineral Petrol* 116:433–447
  59. Ravna K (2000) The Grt-Cpx Fe<sup>2+</sup>-Mg geothermometer: an update calibration. *J Metamorph Geol* 18:211–219
  60. Kohn S (1990) Two new geobarometers for garnet amphibolites with applications to Southeastern Vermont. *Am Miner* 75:89–96
  61. Schmidt MW (1992) Amphibole composition in tonalite as a function of pressure: an experimental calibration of the Al-hornblende barometer. *Contrib Miner Petrol* 110:304–310
  62. Wones DR, Eugster HP (1965) Stability of biotite: experiment, theory, and application. *Am Mineral* 50:1228–1272
  63. Heier KS (1973) Geochemistry of granulite facies rocks and problems of their origin. *Phil Trans Roy Soc Lond Petrol* 55:279–292
  64. Anderson JL, Smith DR (1995) The effect of temperature and oxygen fugacity on Al-in-hornblende barometry. *Am Miner* 80:549–559
  65. Ridolfi F, Renzulli A, Puerini M (2010) Stability and chemical equilibrium of amphibole in calc-alkaline magmas: an overview, new thermobarometric formulations and application to subduction-related volcanos. *Contrib Miner Petrol* 160:45–66
  66. Otten MT (1984) The origin of brown hornblende in the Artfjället gabbro and doerite. *Contrib Miner Petrol* 86:189–199
  67. O'Neill HSC, Pownceby MI (1993) Thermodynamic data from redox reactions at high temperatures. An experimental and theoretical assessment of the electrochemical method using stabilized zirconia electrolytes, with revised values for the Fe–FeO, Co–CoO, Ni–NiO and Cu–Cu<sub>2</sub>O oxygen buffers, and new data for the W–WO<sub>2</sub> buffer. *Contrib Miner Petrol* 114(3):296–314.72
  68. Irvine TN, Baragar WRA (1971) A guide to chemical classification of the common volcanic rocks. *Can J Earth Sci* 8:53–548
  69. Middlemost EAK (1975) The basalt clan. *Earth-Sci Rev* 11:337–364
  70. Winchester J, Floyd P (1977) Geochemical discrimination of different magma series and their differentiation products using immobile elements. *Chem Geol* 20:325–343
  71. Le Bas MJ, Le Maitre RW, Streckeisen A, Zanettin B (1986) A chemical classification of volcanic rocks based on the total alkali-silica diagram. *J Petrol* 27(3):745–750
  72. Sun SS, McDonough WF (1989) Chemical and isotopic systematics of oceanic basalts: implications for mantle composition and processes. In: Saunders AD, Norry M (eds) *Magmatism in ocean basins*, vol 42. Geological Society of London Special Publication, London, pp 313–345
  73. McDonough WF, Sun S-S (1995) The composition of the earth. *Chem Geol* 120:223–253
  74. Sawyer EW (1991) Disequilibrium melting and the rate of melt-residuum separation during migmatization of mafic rocks from the Grenville Front, Quebec. *J Petrol* 32:701–738
  75. Jurewicz SR, Watson EB (1984) Distribution of partial melt in a felsic system: the importance of surface energy. *Contrib Mineral and Petrol* 85:25–29

76. Minyem D, Nédélec A (1990) Origine et évolution métamorphique des gneiss d'Eséka (SW Cameroun) 15<sup>th</sup> Colloquium or African Geology CIFEG, University of Nancy I
77. Weber F, Gauthier-Lafaye F, Whitechurch H, Ulrich M, El Albani A (2016) The 2-Ga Eburnean Orogeny in Gabon and the opening of the Francivilian intracratonic basins: a review. *Compt Rendus Geosci* 348:572–586
78. Beard J, Lofgren G (1991) Partial melting of basaltic and andesitic green-stones and amphibolites under dehydration melting and water-saturated conditions at 1, 3, and 6.9 kilobars. *J Petrol* 32:365–401
79. Atherton MP, Petford N (1993) Generation of sodium-rich magmas from newly underplated basaltic crust. *Nature* 362(6416):144–146
80. Xiong XL, Xian-Hua LI, Ji-Feng XU, Wu-Xian LI, Zhao ZH, Wang Q, Chen XM (2003) Extremely high-Na adakite-like magmas derived from alkali-rich basaltic underplate: the late cretaceous Zhantang Andesites in the Huichang Basin, SE China. *Geochemistry J* 37(2):233–252
81. Floyd P, Leveridge B (1987) Tectonic environment of the Devonian Gramscatho basin South Corn wall: framework mode and geochemical evidence from turbidic sandstones. *J Geol Soc Lond* 144(4):531. <https://doi.org/10.1144/gsjgs.144.4.0531>
82. D'Orazio M, Innocenti F, Manetti P, Haller MJ (2004) Cenozoic back-arc magmatism of the southern extra-Andean Patagonia (44°30'–52°S): a review of geochemical data and geodynamic interpretations. *Revista de la Asociación Geológica Argentina* 59:525–538
83. Thompson RN, Morrison MA, Hendry GL, Parry SJ (1984) An assessment of the relative role of crust and mantle in magma genesis: an elemental approach. *Phil Trans Roy Soc Lond A* 310:549–590
84. Kepezhinkas P, McDermott F, Defant MJ, Hochstaedter A, Drummond MS (1997) Trace element and Sr–Nd–Pb isotopic constraints on a three component model of Kamchatka Arc petrogenesis. *Geochim Cosmochim Acta* 61(3):577–600
85. La Flèche MR, Camire G, Jenner GA (1998) Geochemistry of post-Acadian, Carboniferous continental intraplate basalts from the Maritimes Basin, Magdalen islands, Quebec, Canada. *Chem Geol* 148:115–136
86. Plank T, Langmuir CH (1998) The geochemical composition of subducting sediment and its consequences for the crust and mantle. *Chem Geol* 145:325–394
87. Singh PK, Verma SK, Moreno JA, Singh VK, Malviya VP, Oliveira EP, Arima M (2019) Geochemistry and Sm–Nd isotope systematics of mafic-ultramafic rocks from the Babina and Mauranipur greenstone belts, Bundelkhand Craton, India: implications for tectonic setting and Paleoproterozoic mantle evolution. *Lithos* 330–331:90–107. <https://doi.org/10.1016/j.lithos.2019.02.010>
88. McLennan SM (2001) Relationships between the trace element composition of sedimentary rocks and upper continental crust. *Geochem Geophys Geosyst* 2:1021–1045
89. Zhao JH, Zhou MF (2007) Geochemistry of Neoproterozoic mafic intrusions in the Panzhihua district (Sichuan Province, SW China): implications for subduction-related metasomatism in the upper mantle. *Precamb Res* 152:27–47
90. Meschede M (1986) A method of discrimination between different types of mid-ocean ridge basalts and continental tholeiites with the Nb–Zr–Y diagram. *Chem Geol* 56:207–218
91. Szilas K, Tusch J, Hoffmann JE, Garde A, Munker C (2016) Hafnium isotope constraints on the origin of Mesoarchaeo-andesites in southern West Greenland, North Atlantic Craton. In: Halla J, Whitehouse MJ, Ahmad T, Bagai Z (eds) *Crust–mantle interactions and granitoid diversification Insights from archaeoan cratons*. Geological Society of London, London, p 449
92. Tommasini S, Avanzinelli R, Conticelli S (2011) The Th/La and Sm/La conundrum of the Tethyan realm lamproites; Earth planet. *Sci Lett* 301:469–478
93. Kouamelan AN, Delor C, Peucat JJ (1997) Geochronological evidence for reworking of Archean terrains during the early Proterozoic (2.1 Ga) in the western Côte d'Ivoire (Man Rise–West African Craton). *Precamb Res* 86:177–199
94. Cocherie A, Legendre O, Peucat JJ, Kouamelan AN (1998) Geochronology of polygenetic monazites constrained by in situ electron microprobe Th–U–total lead determination. Implications for lead behaviour in monazite. *Geochim Cosmochimica Acta* 62:2475–2497
95. Cocherie A, Albarède F (2001) An improved U–Th–Pb age calculation for electron microprobe dating of monazite. *Geochim Cosmochimica Acta* 65:4509–4522
96. Aguilar C, Alkmim FF, Lana C, Farina F (2017) Paleoproterozoic assembly of the São Francisco craton, SE Brazil: new insights from U–Pb titanite and monazite dating. *Precamb Res* 289:95–115
97. Thiéblemont D, Goujou JC, Egal E, Cocherie A, Delor C, Lafon JM, Fanning CM (2004) Archean evolution of the Leo Rise and its Eburnean reworking. *J Afr Earth Sci* 39:97–104
98. Gapais D, Potrel A, Machado N, Hallot E (2005) Kinetics of long-lasting paleoproterozoic transpression within the Thompson Nickel Belt, Manitoba, Canada. *Tectonics* 24:1–16

**Publisher's Note** Springer Nature remains neutral with regard to jurisdictional claims in published maps and institutional affiliations.